Contributions to Mineralogy and Petrology (2018) 173:100
https://doi.org/10.1007/s00410-018-1531-9

ORIGINAL PAPER

Textural evolution of perovskite in the Afrikanda alkaline–ultramafic complex, Kola Peninsula, Russia

Naomi J. Potter[1] · Matthew R. M. Ferguson[1] · Vadim S. Kamenetsky[1] · Anton R. Chakhmouradian[2] · Victor V. Sharygin[3,4] · Jay M. Thompson[1] · Karsten Goemann[5]

Received: 10 July 2018 / Accepted: 9 November 2018

Abstract

Perovskite is a common accessory mineral in a variety of mafic and ultramafic rocks, but perovskite deposits are rare and studies of perovskite ore deposits are correspondingly scarce. Perovskite is a key rock-forming mineral and reaches exceptionally high concentrations in olivinites, diverse clinopyroxenites and silicocarbonatites in the Afrikanda alkaline–ultramafic complex (Kola Peninsula, NW Russia). Across these lithologies, we classify perovskite into three types (T1–T3) based on crystal morphology, inclusion abundance, composition, and zonation. Perovskite in olivinites and some clinopyroxenites is represented by fine-grained, equigranular, monomineralic clusters and networks (T1). In contrast, perovskite in other clinopyroxenites and some silicocarbonatites has fine- to coarse-grained interlocked (T2) and massive (T3) textures. Electron backscatter diffraction reveals that some T1 and T2 perovskite grains in the olivinites and clinopyroxenites are composed of multiple subgrains and may represent stages of crystal rotation, coalescence and amalgamation. We propose that in the olivinites and clinopyroxenites, these processes result in the transformation of clusters and networks of fine-grained perovskite crystals (T1) to mosaics of more coarse-grained (T2) and massive perovskite (T3). This interpretation suggests that sub-solidus processes can lead to the development of coarse-grained and massive perovskite. A combination of characteristic features identified in the Afrikanda perovskite (equigranular crystal mosaics, interlocked irregular-shaped grains, and massive zones) is observed in other oxide ore deposits, particularly in layered intrusions of chromitites and intrusion-hosted magnetite deposits and suggests that the same amalgamation processes may be responsible for some of the coarse-grained and massive textures observed in oxide deposits worldwide.

Keywords Coalescence · Recrystallization · Perovskite · Afrikanda · U–Pb ages · Electron backscatter diffraction · Kola Peninsula · Re-equilibration · Oxide deposit

Communicated by Gordon Moore.

Electronic supplementary material The online version of this article (https://doi.org/10.1007/s00410-018-1531-9) contains supplementary material, which is available to authorized users.

✉ Naomi J. Potter
pottern@utas.edu.au

[1] Earth Sciences and CODES, University of Tasmania, Hobart, TAS 7001, Australia

[2] Department of Geological Sciences, University of Manitoba, Winnipeg, MB R3T 2N2, Canada

[3] V.S. Sobolev Institute of Geology and Mineralogy SB RAS, Koptyuga Prospect 3, Novosibirsk 630090, Russia

[4] Novosibirsk State University, Ul. Pirogova 2, Novosibirsk 630090, Russia

[5] Central Science Laboratory, University of Tasmania, Hobart, TAS 7001, Australia

Introduction

Oxide deposits formed by a range of magmatic, metamorphic and sedimentary processes (Borrok et al. 1998; Force 1991; Hou et al. 2017; Irvine 1977; Latypov et al. 2017) are important sources of economically critical elements, like Cr, Fe, V, Ti and platinum group metals. Perovskite ($CaTiO_3$) is not currently mined but could be a significant future titanium resource. This mineral is a typical accessory phase in a range of ultramafic and silica-undersaturated alkaline rocks, such as kimberlites, melilitolites, foidolites and carbonatites (Campbell et al. 1997; Chakhmouradian and Mitchell 1997; Nielsen 1980). In rare cases, perovskite is an abundant rock constituent, such as bebedourites in the Salitre alkaline complex, Brazil (Barbosa et al. 2012), dunites in the Gardiner carbonatite complex, Greenland (Campbell et al. 1997;

Published online: 17 November 2018

Nielsen et al. 1997), and Benfontein kimberlite sills in South Africa (Dawson and Hawthorn 1973). However, perovskite deposits of significant tonnage and grade are exceptionally rare; the few examples, where the economic potential of the perovskite mineralisation has been explored are structurally and texturally complex alkaline–ultramafic intrusions at Afrikanda in northwestern Russia (Herz 1976), Tapira in southeastern Brazil (Brod 1999), and Powderhorn in Colorado, USA (Armbrustmacher 1981). It remains uncertain how the perovskite accumulated to ore-grade levels in these settings.

Scarcity of perovskite ore deposits has not entailed many genetic studies. Several scenarios have been proposed to account for perovskite-rich zones, the most common involves magmatic layering due to gravitational settling (Brod 1999; Dawson and Hawthorn 1973). On the other hand, perovskite-rich segregations show textural similarities to other oxide deposits, so genetic models for oxide ores may be pertinent to the genesis of perovskite accumulations. Relevant models include in situ crystallisation (Charlier et al. 2006; Latypov et al. 2013; Pang et al. 2007; Vukmanovic et al. 2013), magma mixing (Eales et al. 1990; Irvine 1977; Kinnaird et al. 2002), liquid immiscibility (Kolker 1982; Lister 1966; McDonald 1965; Zhou et al. 2005), mobilization of cumulate suspension from staging magma reservoirs (Eales and Costin 2012; Mondal and Mathez 2006), and a range of post-magmatic ore-forming processes, including post-cumulus growth (Vidyashankar and Govindaiah 2009; Yudovskaya and Kinnaird 2010) and deposition from hydrothermal fluids (Cawthorn 2011; Harlov et al. 2016; Knipping et al. 2015; Pushkarev et al. 2015). The current array of contrasting genetic models for the formation of oxide deposits suggests that sources of metals and mechanisms of their accumulation are not exclusive and should not be pigeonholed.

Our study of perovskite from the Afrikanda alkaline–ultramafic complex targets the understanding of mechanisms responsible for the development of related massive ore textures. We describe the mineral assemblages and textures of the main Afrikanda lithologies and define three key perovskite textural types and associated chemical trends. We discuss the stages of perovskite textural development in the ultramafic rocks at Afrikanda, and the possibility of similar processes operating in other oxide deposits worldwide.

Geological background

The Afrikanda alkaline–ultramafic complex is one of the smallest intrusions in the Devonian (~ 380 Ma) Kola Alkaline Province that hosts more than twenty plutonic and subvolcanic bodies, including alkaline, ultramafic, carbonatite, and melilitolite suites (Kukharenko et al. 1965). The Afrikanda complex is a multiphase intrusion emplaced into Archaean gneisses of the Belomorian Mobile Belt during rifting of the Fennoscandian Shield (Chakhmouradian and Zaitsev 1999; Kramm et al. 1993). The complex has a ~ 11.5 km^2 circular shape at the current level of erosion, identified with gravimetric data as a 5 km thick ellipsoidal composite body with a NW-dipping conduit (Arzamastsev et al. 2000; Chakhmouradian and Zaitsev 2004). The complex has a concentric internal structure (Afanasyev 2011; Kukharenko et al. 1965) and hosts texturally and modally diverse olivinites and clinopyroxenites, cross-cut by minor intrusions of carbonatitic and foidolitic rocks (Chakhmouradian and Zaitsev 2004).

The olivinites and minor melilite-bearing olivinites are found as xenoliths (up to 7 m) in the clinopyroxenites, implying that the former rocks represent the earliest intrusive phase at Afrikanda (Chakhmouradian and Zaitsev 1999). The term "olivinites" is used to emphasize that magnetite and perovskite, not chromite, are the major opaque minerals and to maintain consistency with previously published work on Afrikanda and other complexes in the Kola Alkaline Province and petrogenetically similar igneous provinces elsewhere in Russia. Most of the intrusion is composed of texturally and compositionally diverse clinopyroxenites (Chakhmouradian and Zaitsev 2004). These clinopyroxenites are coarse-grained in the centre and transition outwards from fine-grained to nepheline-bearing along the margins, before grading to melteigites. The perovskite ore and perovskite-bearing rocks are hosted in the coarse-grained clinopyroxenites, referred to in the Russian literature as "ore pyroxenites", located in the central part of the complex. The ultramafic rocks often exhibit alternating oxide- and silicate-rich layers that are considered to represent igneous layering (Chakhmouradian and Zaitsev 2004). The oxide layers are primarily composed of perovskite and titanomagnetite and are enriched in rare earth elements (REE) (Chakhmouradian and Zaitsev 2004; Yudin and Zak 1971).

A carbonatitic suite, also known as calcite–amphibole–clinopyroxene rocks, occurs in the central part of the complex as branching veins (2 cm to 2 m thick) and seemingly irregular (in outcrop) bodies that cross-cut the ultramafic series (Chakhmouradian and Zaitsev 1999). According to the field, geochemical and mineralogical evidence, carbonatitic rocks are distinct from the clinopyroxenites, despite the abundance of diopside and perovskite in both. The carbonatitic rocks are mostly massive and coarse-grained to pegmatitic with modal proportions that change considerably over a short distance, producing a succession from silicocarbonatites to calcite carbonatites (Chakhmouradian et al. 2008; Chakhmouradian and Zaitsev 2004; Pekov et al. 1997). The silicocarbonatites show a widespread mineralogical variability on a small spatial scale (Chakhmouradian et al. 2008; Chakhmouradian and Zaitsev 1999, 2002, 2004; Zaitsev and Chakhmouradian 2002). Alkaline feldspathoidal

rocks appear to be the last intrusive phase and are principally represented by the melteigite–urtite series. The bulk of these rocks is associated with the nepheline-bearing clinopyroxenites in the eastern part of the complex, but pegmatoid ijolites comprising major nepheline, magnetite, perovskite and, locally, biotite also occur in the core as dikes cross-cutting the ultramafic and carbonatitic rocks (Chakhmouradian and Zaitsev 1999).

The Afrikanda perovskite-magnetite deposit is confined to the central part of the complex, dominated by coarse-grained clinopyroxenites (> 50%) that host blocks of olivinites and are cross-cut by carbonatitic and feldspathoidal rocks. The ore comprises 15–35 vol% Ti-rich magnetite and 10–36 vol% perovskite, and shows wide variations in the abundance of silicate minerals and calcite, reflecting extreme petrographic heterogeneity of this deposit. The measured reserves, delineated to a depth of 300 m, include 34.3 Mt of ore averaging 12.5 wt% Fe and 8.3 wt% TiO_2 (Afanasyev 2011).

Methodology

All instruments used for the characterisation of samples are housed at the University of Tasmania, Australia. Polished samples were analysed by backscattered electron (BSE) imaging, energy dispersive X-ray spectrometry (EDS) and electron backscatter diffraction (EBSD) using a Hitachi SU-70 field emission scanning electron microscope (SEM) in the Central Science Laboratory. The SEM is fitted with an Oxford XMax80 EDS detector and an HKL Nordlys Nano EBSD camera. Major and trace element and U–Pb isotope analyses of perovskite and titanite were conducted using an Agilent 7900 quadrupole ICPMS, coupled to a Coherent COMPex Pro 193 nm ArF excimer laser system equipped with a Laurin Technic (Resolution S155) constant geometry ablation cell at the School of Earth Sciences. Additional details are provided in the Appendix.

Petrography of rock units

Melilite-bearing olivinites

Melilite-bearing olivinites are fine- to medium-grained, inequigranular rocks composed of forsterite (0.3–2 mm), åkermanite (0.6–2.7 mm), perovskite (50–550 μm) and magnetite (0.2–1.5 mm), and cut by calcite and wollastonite veinlets. Inclusions of euhedral perovskite (30–200 μm) are also found in all other minerals. Perovskite grains are physically separated by serpentine. The preferential orientation of elongate forsterite and magnetite grains and ubiquitous serpentine in the same orientation defines a weak planar fabric in the rock. The interconnected networks and clusters of smaller euhedral perovskite grains enclose and distort the anhedral åkermanite, forsterite and magnetite grains generating intergrown, irregular and concave shapes (Fig. 1a). Åkermanite is sodium-rich (2–3 wt% Na_2O) with thin rims of monticellite (11–12 wt% FeO) surrounding some crystals. The

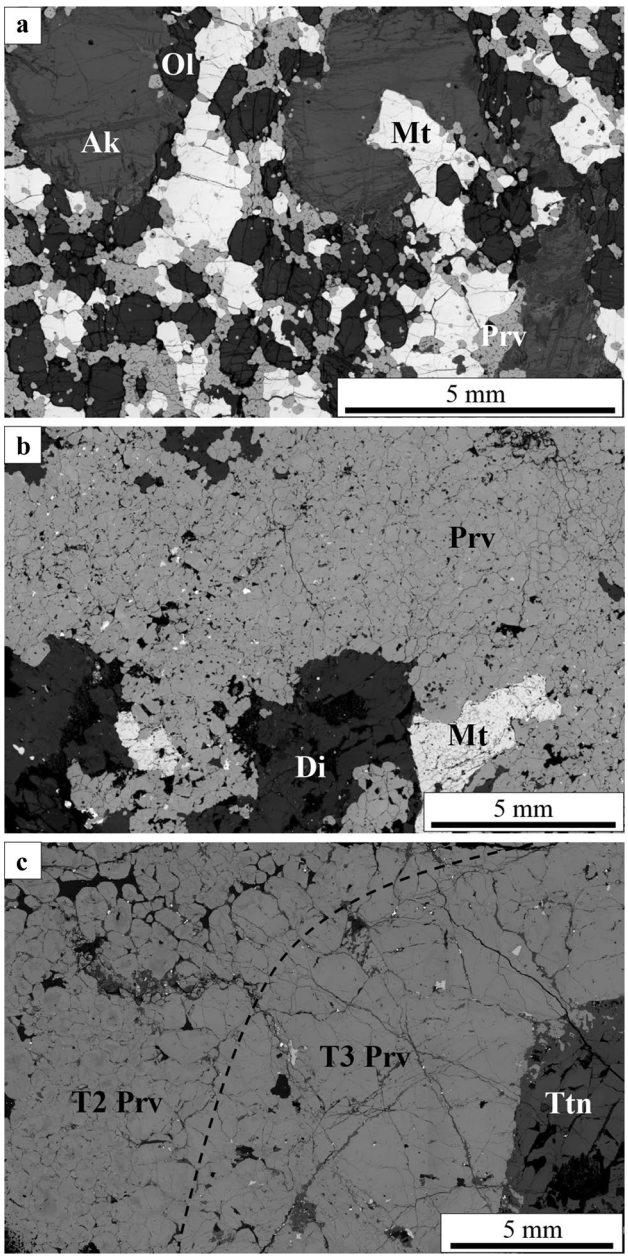

Fig. 1 Backscattered electron (BSE) images of characteristic textures and mineralogy of the three main Afrikanda rock types. **a** Olivinites composed of large akermanite, olivine and magnetite grains enclosed by smaller perovskite grains. **b** Clinopyroxenite composed of diopside, magnetite and smaller perovskite grains. **c** silicocarbonatite composed of perovskite, calcite and titanite. *Ak* akermanite, *Ttn* titanite, *Prv* perovskite, *Mt* magnetite, *Ol* olivine, *Di* diopside

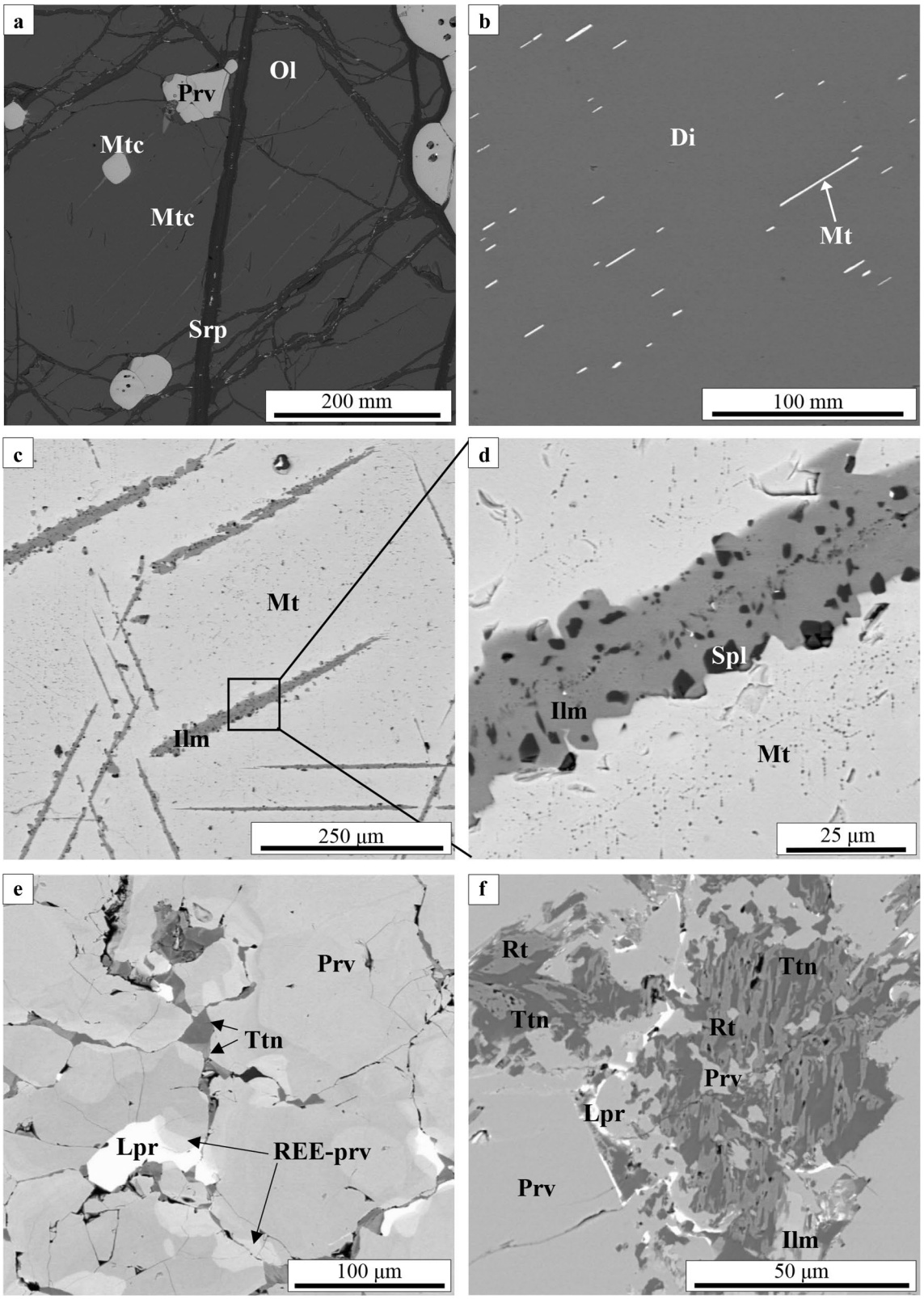

forsterite crystals (~ $Fo_{86–88}$) contain up to 1 wt.% CaO and are partially replaced and cross-cut by serpentine with magnetite infill. Ferroan monticellite lamellae are observed within a few olivine grains (Fig. 2a). Magnetite is compositionally homogeneous with high Ti, Mg and Al contents (4–7, 1–2 and 1–2 wt% respective oxides).

◂**Fig. 2** BSE images of textural features in the Afrikanda rocks. **a** Ferroan monticellite lamellae in olivine from olivinites. **b** Titanomagnetite lamellae in diopside from clinopyroxenite. **c** Mg-rich ilmenite lamellae in magnetite from clinopyroxenite. **d** Close up of **c** with small crystals of ferroan Ti-rich spinel and baddeleyite (white specs) in the Mg-rich ilmenite lamellae. **e** Titanite, REE-perovskite and loparite at T2 perovskite grain margins from clinopyroxenite. **f** Symplectite-like intergrowths of titanite, rutile and ilmenite in T2 perovskite from silicocarbonatite. *Ttn* titanite, *Lpr* loparite, *Prv* perovskite, *Ilm* ilmenite, *REE-prv* REE-rich perovskite, *Mt* magnetite, *Spl* spinel, *Di* diopside, *Mtc* monticellite, *Rt* rutile, *Srp* serpentine, *Ol* olivine

Clinopyroxenites

The examined clinopyroxenites are fine- to medium-grained, inequigranular rocks mainly composed of clinopyroxene, perovskite and magnetite with minor calcite, richterite, phlogopite, magnesiohastingsite, titanite, chlorite and various REE minerals (Fig. 1b). Diopside (0.2 to 1 mm) is zoned with titanomagnetite and magnesiohastingsite lamellae (Fig. 2b) and inclusions of calcite, phlogopite and titanite. Diopside is partially replaced by magnesiohastingsite, biotite and clinochlore. Perovskite shows a range in grain sizes (0.05 to more than 2 mm), shapes (rounded to irregular) and zonation (homogeneous to complexly zoned), and varies from chains of euhedral crystals to large areas of interlocking grains. Magnetite grains are rounded (0.3 to 1.3 mm, with rare grains up to 10 mm) and contain variable Ti, Mg and Al contents (< 4, 3 and 2 wt% respective oxides). Magnetite also contains lamellae of Mg-rich ilmenite (Fig. 2c), trellis-like and irregular patches of ferroan spinel (< 25 µm) and Mn- and Mg-rich ilmenite (< 50 µm). The Mg-rich ilmenite lamellae contain small crystals of ferroan Ti-rich spinel (1 to 3 µm) and baddeleyite (< 1 µm) (Fig. 2d). REE phases are observed as inclusions in other minerals, with ancylite-(Ce) in richterite, cerite-(Ce) in calcite, and ancylite-(Ce), cerite-(Ce) and loparite-(Ce) in titanite.

Silicocarbonatites

The examined silicocarbonatite samples are extremely inequigranular (fine- to coarse-grained) and predominantly composed of calcite, diopside, perovskite, magnetite, magnesiohastingsite and titanite. In perovskite-rich areas, calcite occurs as veinlets (up to 5 mm in width), euhedral crystals (0.3 to > 4 mm across) and interstitial to perovskite (0.3 to 2 mm), and is the most abundant mineral in the samples (up to 50 vol%). Titanite and cerite (less common) are observed at the peripheral areas of the calcite veinlets. Titanite is the most abundant interstitial mineral, with REE minerals such as cerite-(Ce), loparite-(Ce) and ancylite-(Ce) found enclosed in the titanite. Magnetite has low Ti, Mg and Al contents (less than 1 wt%, respectively) and contains lamellae of Mn- and Mg-rich ilmenite and irregular grains of Zn- and Fe-rich spinel. Perovskite shows a range of grain sizes (0.05 to more than 2 mm), shapes (rounded to irregular), and zonation (homogeneous to complexly zoned), and varies from small interlocking grains to large areas of massive perovskite (Fig. 1c). Perovskite also occurs as clusters with accessory titanite, calcite, loparite-(Ce) and rare fluorapatite. For more detailed descriptions of the mineralogy and textures of silicocarbonatites, the reader is referred to publications by Chakhmouradian and Zaitsev (1999, 2002, 2004) and Zaitsev and Chakhmouradian (2002).

Perovskite textures

Three distinct perovskite textures are identified in the three main rock types at Afrikanda. These types are defined by their morphology, composition, zoning patterns and abundance of multiphase inclusions (Fig. 3a–f).

Type one (T1) perovskite is observed in the olivinites and clinopyroxenites, characterised by interconnected polygonal crystal clusters and networks. The euhedral pseudo-octahedral perovskite grains (50–550 µm) have straight boundaries with widespread 120° triple-junctions (Fig. 3a). Multiphase inclusions are abundant in grain cores. The number of inclusions is dependent on grain size, with a general trend of more inclusions with increasing grain size. Most of the perovskite grains exhibit no detectable zoning in BSE images, while a small number of grains along the zone of contact with magnetite grains have a lower-AZ rim (AZ = average atomic number). Perovskite T1 in the clinopyroxenites has a greater number of grains with a low-AZ rim along their contact with both adjacent perovskite and magnetite grains. The perovskite grains neighboured by magnetite can also exhibit oscillatory zoning with multiple narrow bands along the grain boundaries (Fig. 3b). The grain boundaries between perovskite are straight, whereas boundaries with other minerals are curvilinear. The perovskite grain boundaries in the melilite olivinites and clinopyroxenites are clearly visible, however, EBSD revealed that some of these grains are a composite of several subgrains, each with slight deviations in crystal orientation (Fig. 4a_{iii}, b_{iii}).

Type two (T2) perovskite in the clinopyroxenites is represented by an intricate mosaic of interlocking anhedral grains (0.1 to 1 mm; Figs. 1b, 3c) and in the silicocarbonatites, by rounded grains (0.2 to > 2 mm) surrounded by interstitial material (Figs. 1c, 3d). Triple junctions are observed between adjacent perovskite grains in the clinopyroxenites, at approximately 120°. Multiphase and monomineralic inclusions of phlogopite, magnetite, loparite-(Ce), calcite, titanite and fluorapatite vary from rare to abundant among the examined samples. Perovskite in the silicocarbonatites contains a greater proportion of monomineralic inclusions and fewer multiphase inclusions than that in the clinopyroxenites. Zoning is prominent in all perovskite grains and

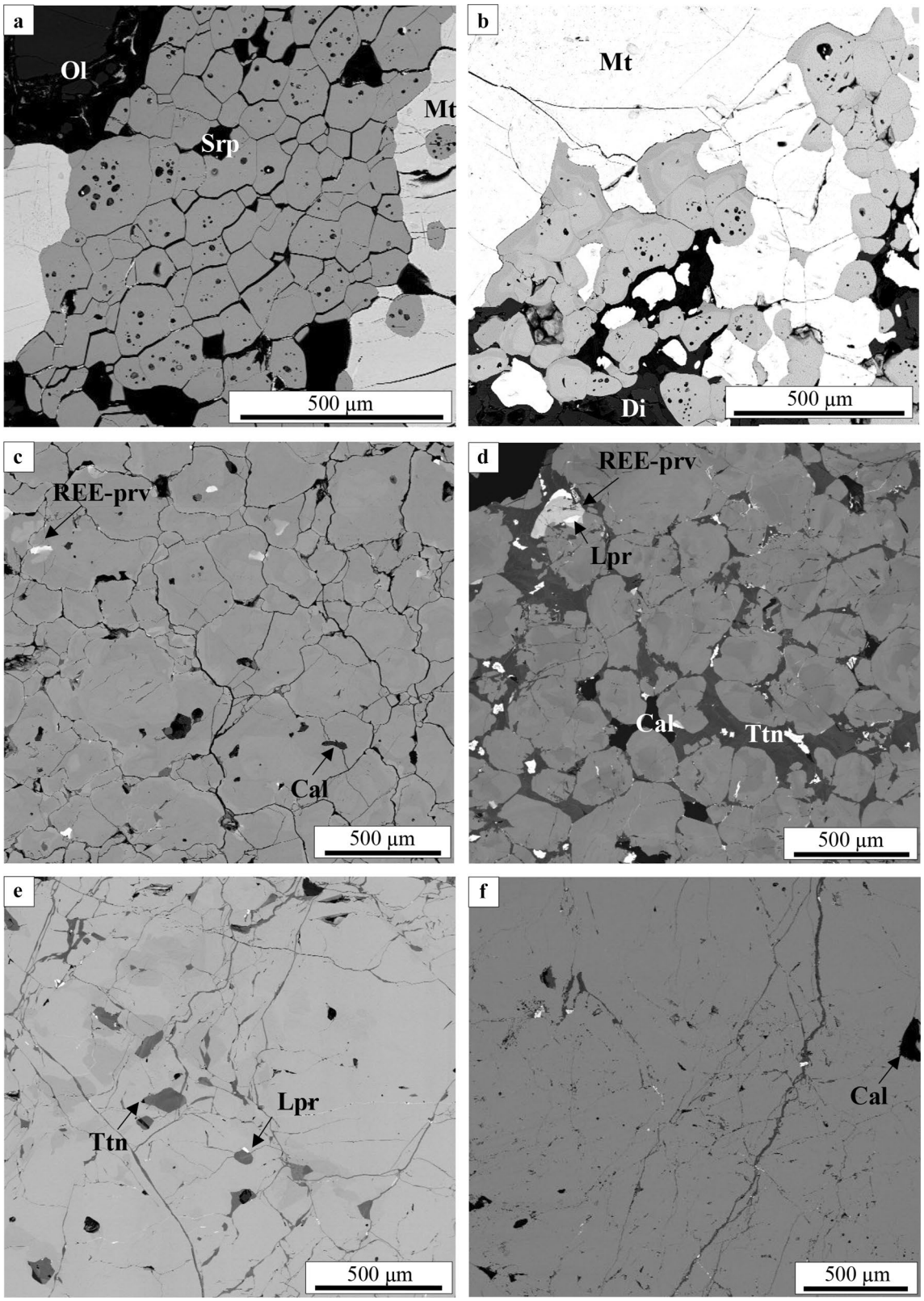

Fig. 3 Representative BSE images of the various perovskite textures. **a** T1 in olivinites. **b** T1 in clinopyroxenite. **c** T2 in clinopyroxenite. **d** T2 in silicocarbonatite. **e** T3 in clinopyroxenite. **f** T3 in silicocarbonatite. *Cal* calcite, *Di* diopside, *Lpr* loparite, *Mt* magnetite, *Ol* olivine, *Srp* serpentine, *REE-prv* REE-perovskite, *Ttn* titanite

can be highly complex in some areas or individual grains. Large grains commonly display less compositional complexity than the smaller grains. The zoning in the core is challenging to decipher due to compositional changes occurring along the grain boundaries and fractures (Figs. 3d, 5a). In BSE images, most grains have a darker core and comparatively lighter rim caused by differences in concentration of Na, light rare earth elements (LREE), and Nb (Fig. 5d). The changes in composition at the rims are not systematic, often showing irregular, embayed patterns (Fig. 5a). In some samples, perovskite has darker rim in areas where perovskite is in direct contact with magnetite or calcite (Fig. 5c).

Distinct areas of perovskite with elevated LREE contents (up to 20 wt%), reflected in their high AZ, are referred to here as REE-perovskite. The mineral ranges in size from 20 µm to 1.5 mm and can exhibit irregular zoning due to differences in Na, LREE and Nb contents (Fig. 3d). The REE-perovskite forms irregular, cuspate shapes as halos around loparite-(Ce) in perovskite and at perovskite rims that are commonly in contact with interstitial loparite-(Ce) and titanite (Fig. 2e). Type 2 perovskite coexists with titanite, calcite and loparite-(Ce); rare fluorapatite was also found in the silicocarbonatites. Titanite is zoned and forms irregular wedge-shaped crystals between perovskite, thin rims around perovskite and intergrown with interstitial ilmenite (0.2-1 mm). REE-perovskite and loparite-(Ce) associated with T2 perovskite are more abundant in the silicocarbonatites, which also contain a larger proportion of interstitial minerals. Perovskite grain boundaries can be difficult to distinguish in BSE images, especially in the silicocarbonatites, however, in the Euler images the boundaries are clearly visible (Fig. 4c_{ii}, d_{ii}). The Euler patterns also show that in the clinopyroxenites, most large irregularly shaped grains have only one crystallographic orientation, while the smaller more-rounded grains still have differences in orientation that indicate the presence of subgrains (Fig. 4c_{iii}). The irregular grain boundaries of large perovskite crystals suggest they developed from multiple smaller grains (Fig. 4c_{ii}). In the silicocarbonatites, the small and large perovskite grains have only one orientation (Fig. 4d_{iii}).

Type 3 (T3) in the clinopyroxenites and silicocarbonatites is represented by massive perovskite with patches of irregular zoning and rare multiphase inclusions. The intensity of the zoning varies across the samples, some areas are almost homogeneous and others exhibit complex patterns due to extreme variations in Na, LREE and Nb contents (Fig. 4b). Chakhmouradian and Zaitsev (1999) also reported small-scale order-of-magnitude variations in Th in REE-perovskite and loparite-(Ce) mantling T3. These authors also described oscillatory growth patterns truncated by Na-REE (±Nb,Th)-rich areas in euhedral cubo-octahedral crystals. Mineral inclusions of titanite, calcite, loparite-(Ce) and cerite are dispersed throughout massive perovskite and between perovskite grains. Generally, areas of perovskite with interstitial minerals contain fewer mineral inclusions, and vice versa. Interstitial titanite can be intergrown with ilmenite and form large patches up to 1 mm containing scattered ilmenite and perovskite. Symplectite-like intergrowths of titanite, rutile and ilmenite (200–500 µm) are typical in some silicocarbonatites (Fig. 2f). Type 3 perovskite lacks easily distinguishable grain boundaries. The Euler images show that perovskite is massive, with the same crystallographic orientation for large areas of perovskite (Fig. 4e_{ii}, f_{ii}).

Multiphase inclusions in perovskite

The perovskite-hosted multiphase inclusions in the three rock types show rounded, elongated and irregular shapes, and range from < 5 to 50 µm across. The inclusions are all identified as primary based on their random/unsystematic distribution within the grains and the lack of association with secondary features, such as healed fractures. The inclusions typically contain three to ten mineral phases and include anhydrous and water-bearing silicates, carbonates, oxides, sulphides and phosphates. The abundance of multiphase inclusions and their mineralogical complexity decrease from the olivinites to clinopyroxenites and then silicocarbonatites. A detailed analysis and discussion on these multiphase inclusions will be presented in a subsequent publication.

Perovskite compositions

The textural types of perovskite in the three rock types vary in major and trace element compositions. The substituent elements show a negative correlation with Ca and Ti and a positive correlation with each other (Fig. 6a–d). Type 1 perovskite has the lowest abundances of substituent elements and a limited range of compositions, notably up to 2 wt% REE and less than 1 wt% Fe (Fig. 6d). The range in element concentrations is greater in T2 and T3 perovskite due to their complex zoning patterns, with the most compositional scatter observed in T2 perovskite from the silicocarbonatites and T3 perovskite from the clinopyroxenites (Fig. 6). Type 2 perovskite contains 1–7 wt% REE and up to 1.5 wt% Nb and Fe, while T3 perovskite has 4–7 wt% REE, 1–2 wt% Nb, and up to 1.5 wt% Na and Fe.

The REE budget of perovskite is dominated by cerium with the abundance of other lanthanides decreasing with increasing atomic number [La > Nd > Pr > Sm; $(La/Yb)_{CN}$ = 140–2300]. Chondrite-normalised REE patterns for all textural types exhibit a negative slope (Fig. 7). Overall, the chondrite profiles show a relative enrichment in all REE from T1 to T3, with a greater increase in light REE for T2 and T3 compared to T1. The complete set of LA-ICPMS data is presented in the Appendix.

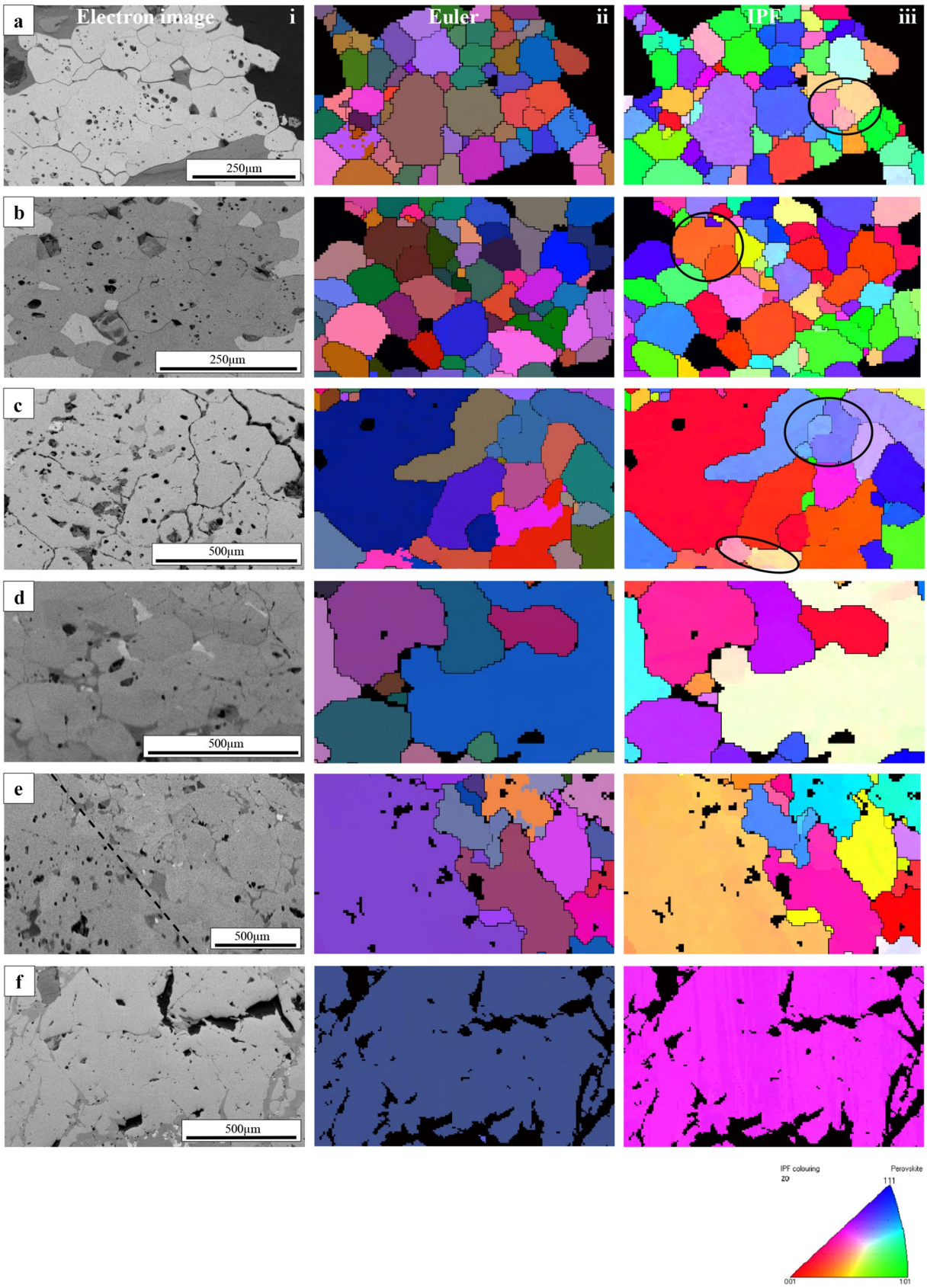
a
Electron image
i
Euler
ii
IPF
iii
250µm
b
250µm
c
500µm
d
500µm
e
500µm
f
500µm
IPF colouring
Z0
Perovskite
111
001
101

◂**Fig. 4** Structural analysis and crystallographic orientation of perovskite grains in the different textures. **a** T1 in olivinites. **b** T1 in clinopyroxenite. **c** T2 in clinopyroxenite. **d** T2 in silicocarbonatite. **e** T2 (right) and T3 (left) in silicocarbonatite. **f** T3 in clinopyroxenite. **i** BSE image of the area mapped with EBSD shows perovskite grain boundaries. **ii** EBSD map representing the orientation of neighbouring perovskite grains in Euler space using colours to denote the variety of crystal orientations in space using Euler angles: φ1-red φ-green, φ2-blue. **iii** Inverse pole figure (IPF) map in the *X* or *Z* direction showing the variation in crystal orientation using colours. Black ovals show grains that are composed of subgrains with different crystallographic orientations

U–Pb geochronology

Fifteen in situ U–Pb isotopic measurements were obtained for perovskite from the olivinites, 45 from the clinopyroxenites and 124 from the silicocarbonatites. All but one analysis were used in age calculations. Perovskite contains abundant common Pb and so concordia intercept ages using the Tera–Wasserburg plot are reported. The Pb isotope composition of calcite was analysed and used as a common-Pb anchor for the concordia intercept ages because this mineral has high Pb/U ratios. The measured $^{207}Pb/^{206}Pb$ value of calcite is 0.8277 ± 0.0039 and, thus, differs from the two-stage Pb evolution model of Stacey and Kramers (1975) for 380 Ma. Perovskite from all lithologies gives a concordia intercept age of 368.3 ± 1.2 +/- 7.48 Ma (including systematic uncertainties) with an MSWD of 0.80 and a probability-of-fit of 0.98 (Fig. 8a). Perovskite ages for each of the analysed lithologies are reported in Table 1.

One hundred and eleven in situ U–Pb isotope analyses of titanite were obtained from the silicocarbonatites. Significant scatter and discordance in the U–Pb system are present. A concordia intercept age of 374.2 ± 5.3 Ma +/- 7.5 Ma (including systematic uncertainties) was calculated for data points, whose concordance was greater than 50%, using the calcite common-Pb anchor (see above; Fig. 8b). The complete set of U–Pb geochronology results is presented in the Appendix.

Discussion

Age of the Afrikanda complex

The Palaeozoic igneous complexes in the Kola Alkaline Province were emplaced during a relatively short time during the Late Devonian (380−360 Ma) with no reliably post-Devonian magmatic events recorded to date (Arzamastsev et al. 2000). The Afrikanda complex was emplaced at ~ 380 Ma with other alkaline–ultramafic complexes, including Kovdor, Turiy Mys, Lesnaya Varaka and Ozernaya Varaka (Arzamastsev and Wu 2014).

Our geochronological study of perovskite from the melilite olivinites, clinopyroxenites and silicocarbonatites yielded similar ages of 370.4 ± 5.4, 368.9 ± 2.9, 368.1 ± 1.3, respectively (Table 1). Our average perovskite age of 368.3 ± 1.2 Ma (Fig. 8a) is in good agreement with most of the previously published U–Pb ages for this intrusion (Fig. 9), including: 364 ± 3 Ma and 374 ± 10 for perovskite from clinopyroxenite (Kramm et al. 1993; Reguir et al. 2010), 371 ± 8 Ma for perovskite from silicocarbonatite (Reguir et al. 2010), and 377 ± 3 Ma for schorlomite from silicocarbonatite (Salnikova et al. 2018). Somewhat older ages were reported by Wu et al. (2010, 2013) for perovskite from clinopyroxenite, calcite-bearing perovskite ore and ijolite–melteigite (376–385 Ma, averaging 381 ± 2 Ma), and for calzirtite and zirconolite from clinopyroxenites (Wu et al. 2010). Several factors could be responsible for the slight age discrepancies between our data and the data of Wu et al. (2010, 2013), including the choice of U–Pb calibration material, susceptibility of some analytical techniques to matrix effects, and the choice of a common-Pb anchor. Our study supports the contemporaneous emplacement of the various rock types (olivinites, clinopyroxenites and silicocarbonatites) in the Afrikanda complex, as indicated by the identical ages of the perovskite from the different lithologies (Fig. 9). Evidence for the relatively rapid emplacement of the Afrikanda deposit comes primarily from the homogeneity of the perovskite U–Pb ages (MSWD of 0.80 for all perovskite analyses), at least at the precision attainable with the LA-ICPMS system used. Additionally, our study presents new insights into the common-Pb isotopic composition of the Afrikanda perovskite and shows that the initial Pb isotopic composition of its parental magma is significantly more radiogenic than predicted by the two-stage model of Stacey and Kramers (1975).

U–Pb age data have not been previously reported for titanite from the Afrikanda complex. Significant scatter in the U–Pb system for titanite is a result of either Pb movement within the titanite structure after crystallisation, or the incorporation of radiogenic and common Pb. Lead loss or partial re-setting of the U–Pb system during later recrystallisation events could also be responsible for some of the scatter (Fig. 8b). Using data whose concordance is better than 50%, an age of 374.2 ± 5.3 Ma was calculated and is consistent with the perovskite results discussed above (Table 1). However, a range of younger titanite ages that are more discordant due to Pb loss suggest there may have been a re-setting or titanite crystallisation event.

Development of perovskite textures

The detailed textural and chemical examination of perovskite in the olivinites, clinopyroxenites and silicocarbonatites

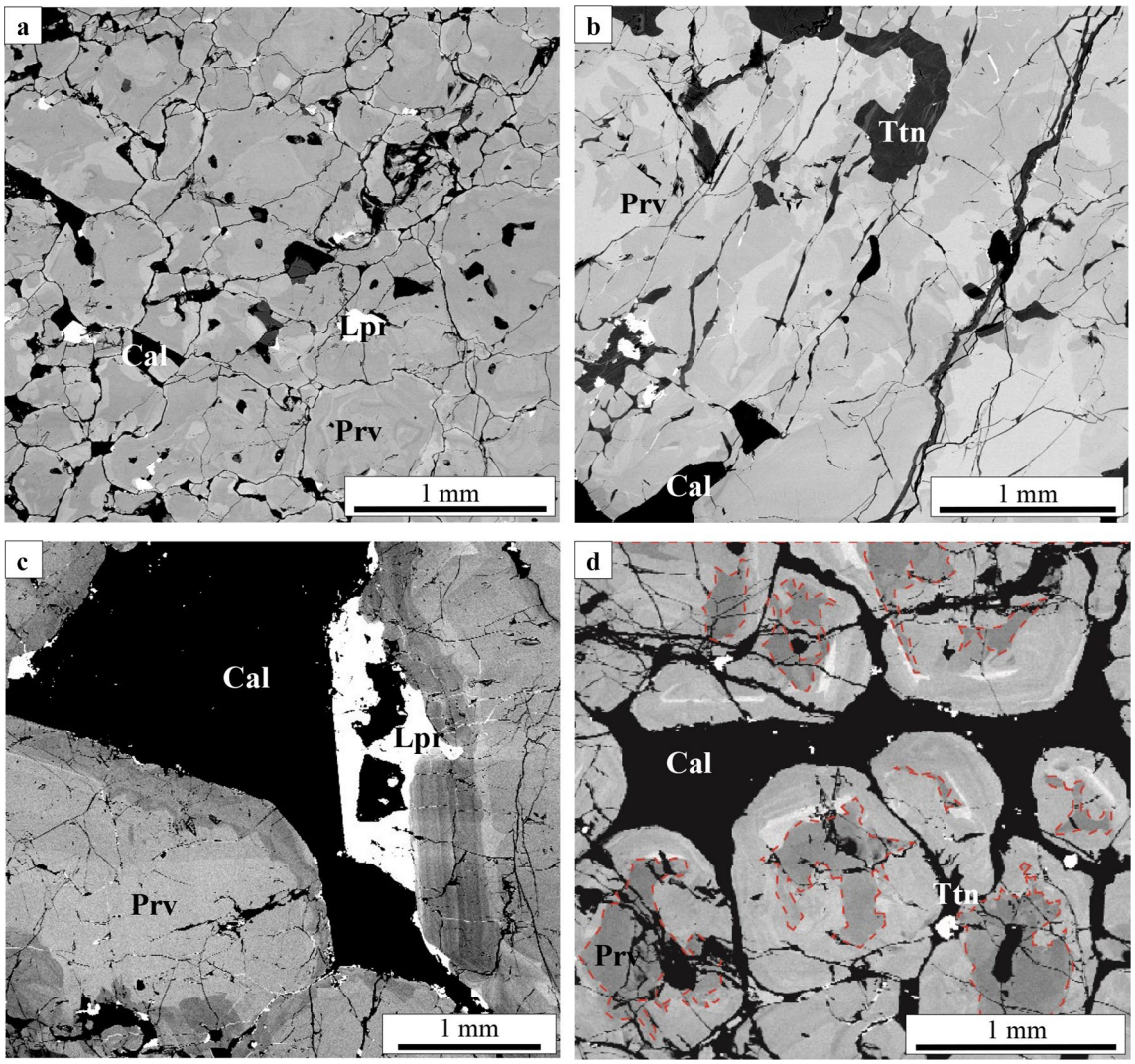

Fig. 5 BSE images of zoning patterns in T2 and T3 perovskite (enhanced contrast in **c, d**). **a** Complex zoning crossing grain boundaries in T2 clinopyroxenite. **b** Irregular zoning pattern in T3 clinopyroxenite. **c** The rims are enriched in REE (rare earth elements) and the cores are depleted in REEs in T2 perovskite in silicocarbonatites. The red dashed lines show the internal extent of zoning. **d** Dark rim (depleted in REE) in contact with calcite and loparite in silicocarbonatite. *Lpr* loparite, *Ttn* titanite, *Prv* perovskite, *Cal* calcite, *REE-prv* REE-perovskite

revealed three perovskite types distinguished by morphology, zonation, inclusion abundance and chemical composition. The olivinites host T1 perovskite (Figs. 1a, 3a), whereas the clinopyroxenites contain T1–3 perovskite (Figs. 1b, 3b–d) and similar T2 and T3 textures are observed in the silicocarbonatites. We have separated the geological interpretation of the ultramafic rocks (discussed below) from that of the silicocarbonatites. The focus here is primarily on the textural evolution of the olivinites and clinopyroxenites, because perovskite textures in the silicocarbonatites have been discussed previously by Chakhmouradian and Zaitsev (1999, 2004).

Olivinites and clinopyroxenites

Textures of rocks are the sum of all processes involved from the initial formation through maturation, and can be used to understand the sequence and nature of each of the evolutionary stages. However, the process of textural equilibration can effectively obscure features related to earlier developmental phases, so we can only speculate from the existing textures about the nature of a rock prior to recrystallization (Pike and Schwarzman 1977). In the case of the Afrikanda rocks, T1 perovskite forms chains and clusters and may suggest that at some point in the early history of the rock individual euhedral grains of perovskite were disseminated and then clumped together to form clusters and chains (Figs. 1a, 3a,

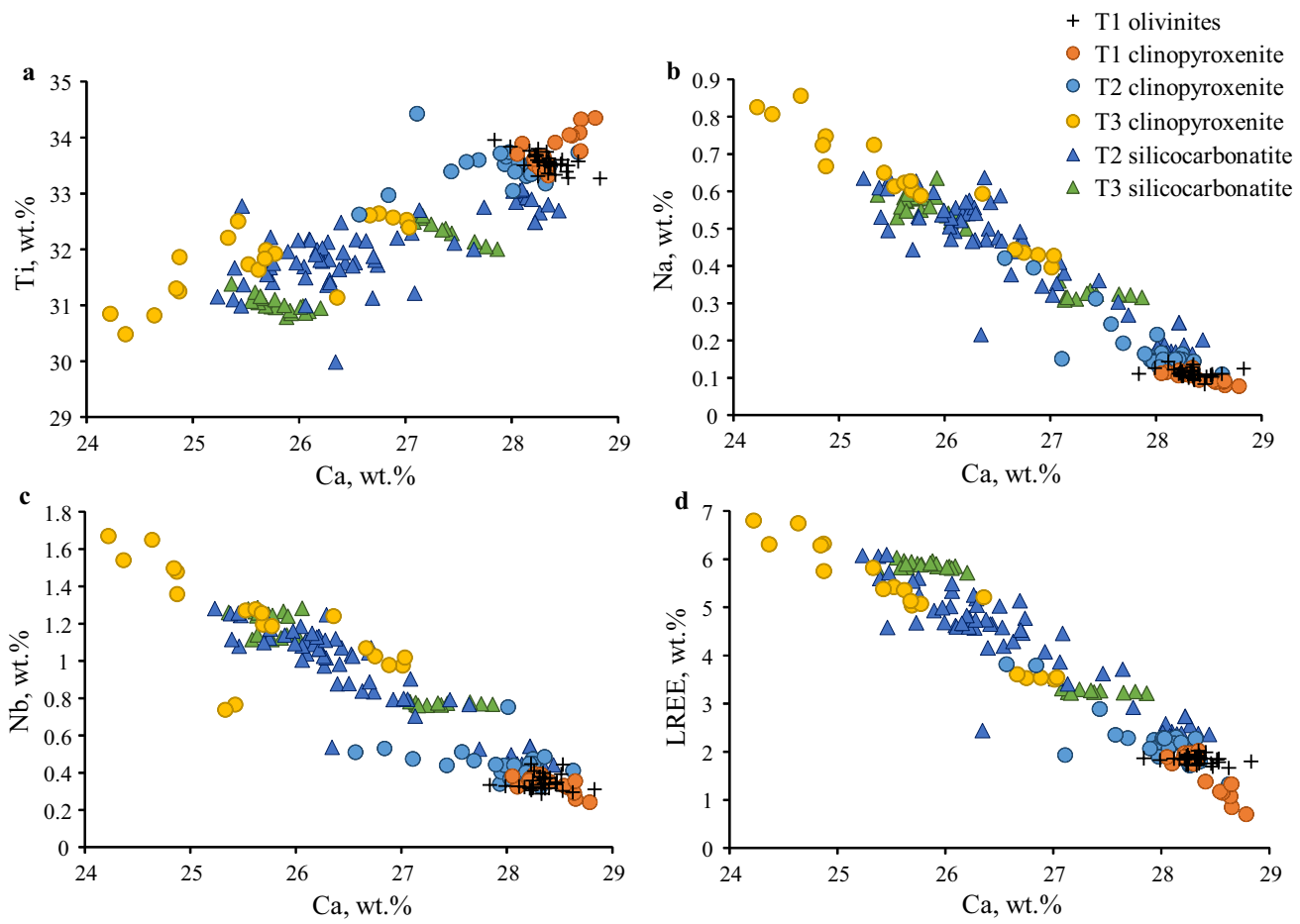

Fig. 6 Bivariate plots of LA-ICPMS major- and trace-element chemistry of the perovskites. Symbols correspond to the four perovskite textures found in the Afrikanda rock types: olivinites (crosses), clinopyroxenites (circles) and silicocarbonatites (triangles)

b). However, we cannot provide clues on the origin of these individual perovskite grains due to the subsequent overprinting events. Therefore, we focus here on development of the Afrikanda perovskite ore by reconstructing the later stages of mineral amalgamation and recrystallization.

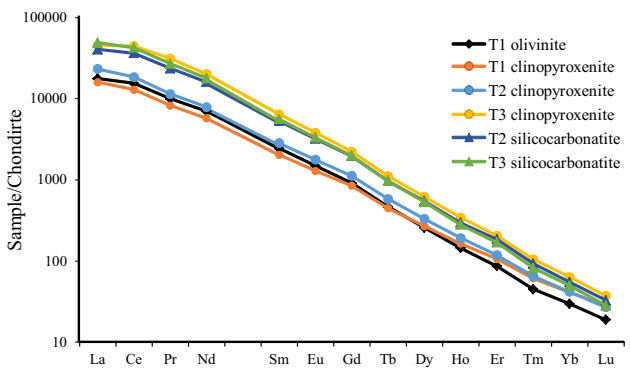

Fig. 7 Chondrite-normalised REE diagram of the average composition of T1 to T3 perovskite in the Afrikanda complex

Textural equilibration

The T1 perovskite aggregates consist of closely packed equigranular crystals with pseudo-octahedral shapes, forming straight boundaries that converge at ~120° triple junctions. This arrangement resembles granoblastic-polygonal textures (Figs. 3a, 10a), as observed in monomineralic cumulates, mantle-derived ultramafics and massive metamorphic rocks such as granofelses (Fig. 10a, b) (Higgins 2011; Holness et al. 2005, 2006; Hunter 1987; Kretz 1966; Wandji et al. 2009). Therefore, we suggest the granoblastic-polygonal texture of T1 perovskite indicates that the host rocks have experienced dynamic textural equilibration. The granoblastic-polygonal texture of T1 perovskite in olivinites and clinopyroxenites differs marginally due to the variable abundance and distribution of the surrounding minerals, with perovskite in

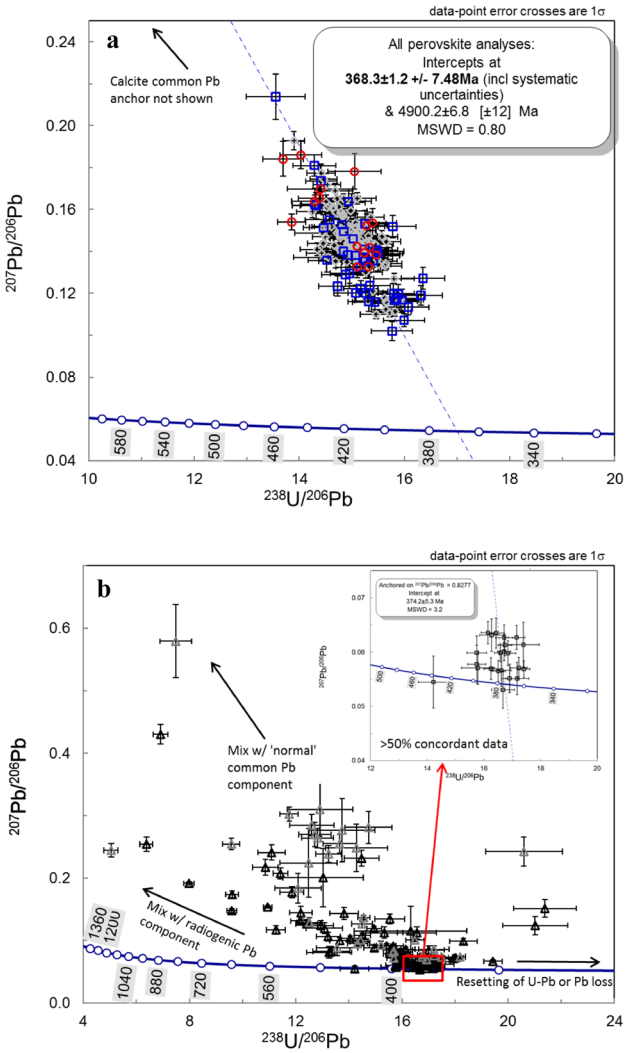

Fig. 8 Tera–Wasserburg concordia plot for **a** perovskite and **b** titanite analyses. Symbols: **a** red circles are olivinites, blue squares are clinopyroxenites, grey diamonds are silicocarbonatites **b** grey and black triangles represent titanite around perovskite in the T3 and T4 silicocarbonatites, respectively. Error crosses are 1 sigma, while concordia intercept ages are 2 sigma. Systematic error component includes uncertainty in decay constants, uncertainty in primary calibration material and excess uncertainty factor of Horstwood et al. (2016)

Table 1 Summary of U–Pb ages of perovskite and titanite from samples of olivinites, clinopyroxenites and silicocarbonatites

Rock type	Mineral	Age (Ma)	MSWD	POF
Olivinite	Perovskite	370.4 ± 5.4/ ± 9.8	1.3	0.19
Clinopyroxenite	Perovskite	368.9 ± 2.9/ ± 7.9	0.84	0.76
Silicocarbonatite	Perovskite	368.1 ± 1.3/ ± 7.5	0.74	0.98
Silicocarbonatite	Titanite	374.2 ± 5.3/ ± 7.5	3.2	0

Uncertainties are 2 sigma absolute and include uncertainties derived from random sources followed by uncertainties from random plus systematic sources of uncertainty calculated according to Horstwood et al. (2016)

POF probability-of-fit

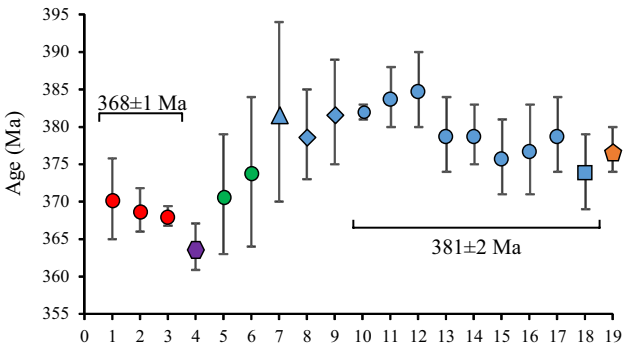

Fig. 9 Age summary of the alkaline ultramafic rocks in the Afrikanda complex. **1–3** Perovskite (circles) analysed in this paper. **4** Whole rock analysis (hexagon) in Kramm et al. (1993). **5–6** Perovskite data in Reguir et al. (2010). **7–9** Calzirtite (triangle) and zirconolite (diamond) data in Wu et al. (2010). **10–18** Perovskite and baddeleyite (square) data in Wu et al. (2013). **19** Schorlomite (pentagon) analysis in Salnikova et al. (2018)

the olivinites clumped together forming aggregates, but dispersed in clinopyroxenites forming chains. Textural equilibration is a well-known phenomenon in natural systems (e.g., Higgins 2015, 2017; Holness et al. 2006), but the bulk of empirical data, computer simulations and models comes from materials research, especially alloys, ceramics and thin films (e.g., Holm et al. 2016). Thus, our current understanding of textural equilibration is limited to relatively simple systems (from a geologist's standpoint) that differ both chemically and mechanically from oxide-silicate assemblages described in the present work. Another challenge in adopting materials science theories to rocks is terminology; for example, their use of the term "recrystallization" is essentially restricted to deformation-induced phenomena, whereas processes addressed in this paper would be described as "grain growth due to annealing" [e.g., Chap. 11 in Humphreys and Hatherly (2004)]. According to previously published experimental evidence, the degree and style of textural equilibration depend on many parameters, notably temperature, pressure, grain distribution, modal homogeneity of the precursor, high-temperature phase transitions, the presence of structural defects, and such kinetic factors as cooling rate (Clark et al. 1977; Humphreys and Hatherly 2004; Kreitcberg et al. 2017; McCloy et al. 2009; Syrenko and Klinishev 1973). Because we observe no evidence for postmagmatic metamorphism at Afrikanda, and the subsolidus mineral assemblages common in the silicocarbonatites record a temperature range of 200–400 °C (Chakhmouradian and Williams 2004; Chakhmouradian and Zaitsev 2004), we assume the documented textural changes arose during cooling. The process involved grain boundary migration, boundary-angle adjustment, dislocation movement, loss of inclusions, and ultimately, coarsening of the grains

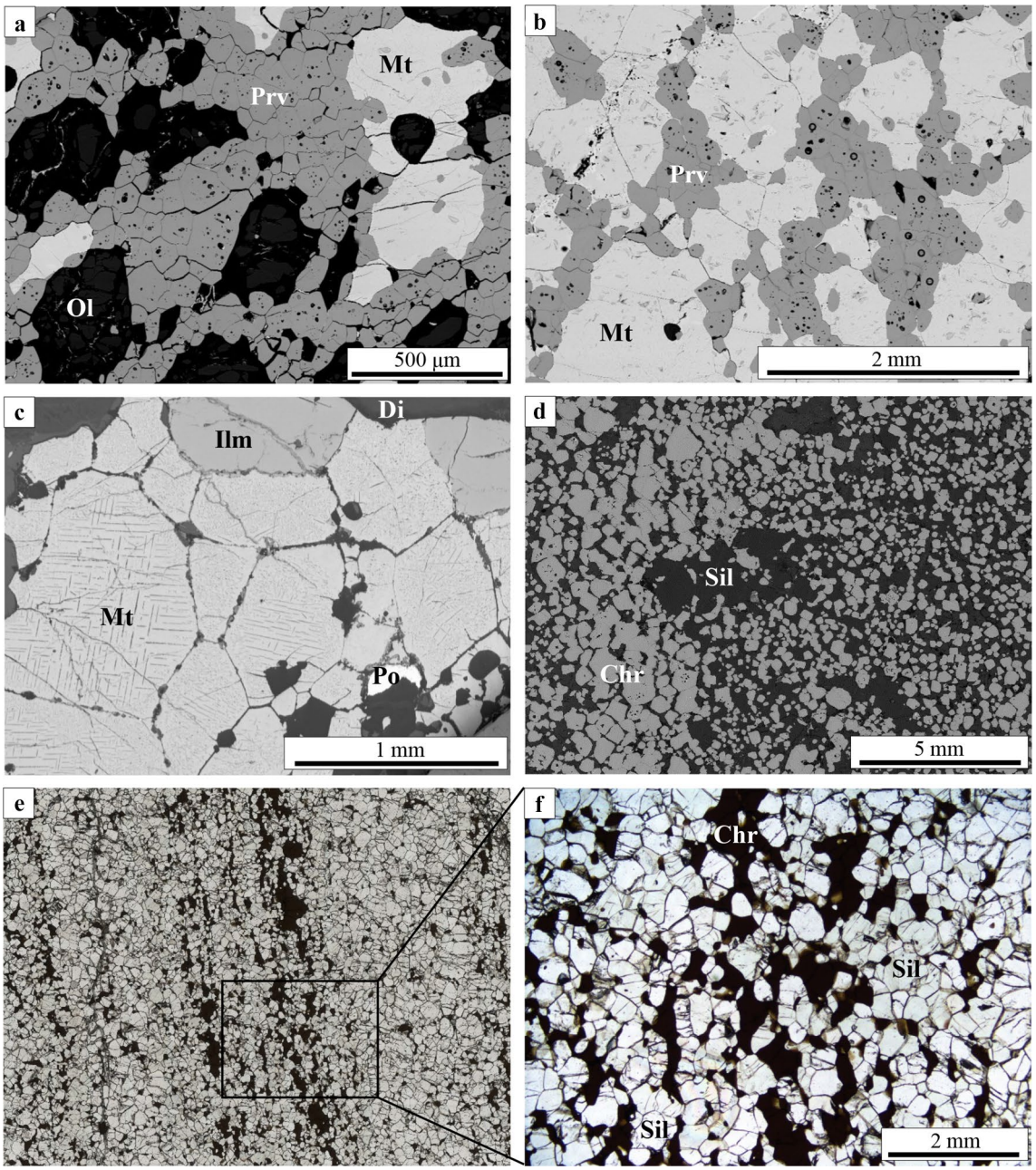

Fig. 10 BSE images of granoblastic textures (**a–d**) SEM (**e, f**) Plane-polarized light. **a** Equigranular mosaic of T1 perovskite from olivinite in the Afrikanda complex with straight boundaries and 120° triple junctions. **b** Perovskite chains of T1 perovskite from clinopyroxenite in the Afrikanda complex. **c** Polygonal grains of Ti-magnetite in an Fe–Ti oxide ore layer at Panzhihua, China. **d** Disseminated equigranular euhedral chromite, with some chains and aggregates from Merensky Reef, South Africa. **e** Chains of chromite grains in a xenolith hosted in a tertiary basalt from the Snowy Mountains, Australia. **f** Close up of (**e**). *Chr* chromite, *Sil* silicate minerals, *Prv* perovskite, *Ilm* ilmenite, *Mt* magnetite, *Di* diopside, *Po* pyrrhotite

to minimise their internal and surface energies (Hunter 1987). We suggest that after perovskite accumulation, slow cooling of the ultramafic rocks enabled the transformation of many small, randomly oriented and possibly irregularly fitted perovskite grains into the observed polygonal mosaics (Figs. 1a, 3a, 10a).

Perovskite coalescence and coarsening

Grain coalescence and coarsening are important processes in the late stages of textural equilibration (Doherty et al. 1997; Hunter 1987). In this section, we discuss grain growth during subsolidus evolution of the ultramafic rocks at Afrikanda as a continuation of the previously recognised textural equilibration. The development of larger grains can either occur by grain boundary migration, i.e., through the dissolution of small crystals and simultaneous growth of larger crystals, or by grain coalescence, where adjacent grain boundaries are eliminated as similarly oriented crystals coalesce (Higgins 2011; Li 1962). The application of EBSD in our study of perovskite enables us to identify and differentiate between these two types of grain growth (Humphreys 2001). Some large grains in T1 and T2 perovskite are composed of subgrains with slightly different crystallographic orientations (circled in Fig. 4a–c). These subgrains within larger perovskite grains suggest the dominant mechanism of grain growth was grain rotation and coalescence. Experimental evidence has shown that coalescence is favoured over grain boundary migration at lower temperatures (Rios et al. 2005; Sandström et al. 1978; Varma and Willits 1984; Walter and Koch 1963). This further supports that the observed perovskite textures and their inferred transformation represent a postmagmatic environment.

The process of grain coarsening occurs via diffusion of vacancies in the crystal lattice, in an effort to eliminate or homogenise high angle, irregular, and large area boundaries (Li 1962). These disequilibrium features are removed as adjacent crystals adopt similar crystallographic orientations and grain boundaries are eliminated as similarly oriented grains coalesce into one larger crystal; this process is exemplified by T1 and T2 perovskite (circled in Fig. 4a–c) (Jones et al. 1979; Li 1962; Rios et al. 2005). These larger grains can continue to grow at low-angle boundaries with neighbouring small grains (Li 1962). Also during coalescence, the new grain boundaries straighten, removing 120° triple junctions by adjusting the dihedral angles of the adjacent grains. This process alters the morphology of the newly coalesced grain and neighbouring grains (see Fig. 4 in Rios et al. (2005)). Triple junctions are typical in T1 perovskite, while less common triple junctions in T2 are no longer strictly at 120° due to the boundary migration associated with grain coalescence (Fig. 3c; Vernon 1970). Type 2 perovskite shows the best examples of grain coalescence, with EBSD images capturing grain coalescence "in progress" (like T1) and at completion. Larger T2 perovskite grains in the clinopyroxenites have some remaining triple junctions and are composed of multiple misoriented subgrains of similar sizes to T1 perovskite (Fig. 4c_{iii}). We suggest the large grains initially resembled T1 perovskite clusters prior to coalescence and have not completely adopted a uniform orientation. Further, we interpret the textural equilibration in the Afrikanda perovskite samples to indicate that coalescence and coarsening of small equilibrated polygonal clusters (T1) enabled the development of a mosaic of larger T2 polycrystalline grains with interlocking grain boundaries and smaller areas of massive T3 perovskite.

Effects of recrystallization

The coarsening of accumulated perovskite during recrystallization in the Afrikanda complex is supported by the complex chemical zoning patterns in perovskite and exsolution lamellae in the associated minerals.

Perovskite chemical zoning

Perovskite-group minerals serve as sensitive indicators to changes in parental environments through complex substitutions of multiple elements in their structure (Chakhmouradian et al. 2013; Mitchell et al. 2017). The variation in the composition and zoning of perovskite from T1 to T3 records the chemical evolution of its crystallisation environment under open- or closed-system conditions. Zoning patterns can be caused by chemical fluctuations in the parental medium, changes in the physical conditions during crystal growth, or solid-state redistribution of elements (Dowty 1976a, b).

Perovskite in T1 is distinguished from T2 and T3 perovskite by the state of textural equilibration and significant differences in chemical composition. Importantly, T1 grains have no internal zoning, consistently low REE values and minor compositional variation localized to the rims of some grains in contact with magnetite (Figs. 3b, 6a–d). Perovskite in the clinopyroxenite shows far more compositional variation, with simple zoning along perovskite grain contacts and oscillatory patterns at the contacts adjacent to magnetite (Fig. 3b). We interpret the internal compositional homogeneity to record textural equilibration of perovskite grains, and the minor zoning to arise from later metasomatic processes.

In contrast, T2 and T3 perovskite are significantly more complex with non-systematic and discontinuous zoning (Fig. 5a, b). Their composition is highly variable, particularly with respect to REE contents (Fig. 6d) and is linked with the irregular and complex zoning patterns. Zoning in T2 and T3 perovskite could be associated with the development of local chemical gradients during grain coalescence, where the differential diffusion of cations creates compositional complexity and irregularity superposed over the existing grain morphology (Fig. 6d). Perovskite in T3 is massive and most of T3 is relatively homogeneous, with some areas still displaying convoluted zoning with no clear pattern (Fig. 3e, f). We suggest these homogeneous areas re-equilibrated through solid-state diffusion removing the

complex zoning and physical impurities such as multiphase inclusions. Areas that are texturally heterogeneous underwent limited textural re-equilibration; however, the zoning is still less complex or abundant than in T2 perovskite.

Controls on perovskite compositions

The composition of T1 perovskite is fairly homogeneous, while T2 and T3 vary significantly, reflecting changes in the availability of such elements as REE, Nb and Th (Fig. 6c, d). In T2 perovskite, these elements are primarily concentrated at the rims and along the grain boundaries (Fig. 2e, 5a, c, d). This type of zoning can be produced by selective cation diffusion during re-equilibration of perovskite with a fluid phase. This process has been invoked to explain perovskite zoning in some kimberlites (Chakhmouradian et al. 2013) and loparite-(Ce) replacement by cation-deficient phases in some alkaline rocks (Chakhmouradian et al. 1999). We suggest the high-REE rims in the Afrikanda T2 perovskite are probably associated with the progressive infiltration of REE and other substituent elements into perovskite from a fluid percolating along grain boundaries and fractures (Fig. 2e). The formation of T3 perovskite was a continuation from T2 polycrystalline grains, and resulted in higher levels of REE (on average) in T3 relative to T2 perovskite from the same rock type (Fig. 7). This enrichment in REE possibly required input of these elements from an external source (e.g., carbonatitic or alkaline magma; Chakhmouradian and Mitchell 1997). We envisage that continuous flux of REE through the ultramafic intrusion under open-system conditions produced the compositional variations.

The presence of REE-perovskite and loparite-(Ce) as discontinuous rims and overgrowths on T2 and T3 perovskite (Figs. 2e, 5a, b) is also undoubtedly linked to the infiltration of a REE-rich fluid in an open system. We agree with Chakhmouradian and Mitchell (1997) that these minerals developed due to infiltration of REE-rich CO_2-rich fluid, which facilitated both fracturing and the uptake of REE ($\pm$ Th $\pm$ Nb) in the perovskite structure. The infiltration of REE into the crystal structure produces a diffuse marginal zone of REE-perovskite (Fig. 2e), whose width is controlled by the kinetics of diffusion and the relative diffusivity of differently charged cations (Chakhmouradian et al. 2013). Similar perovskite–loparite-(Ce) reaction rims and mantles have been reported in other carbonatite complexes and, less commonly, in evolved kimberlites (Chakhmouradian et al. 1999; Chakhmouradian and Mitchell 1997, 2000).

Exsolution lamellae

Exsolution lamellae are a common feature in minerals that have undergone re-equilibration to rid their crystal structure of impurities through solid-state diffusion (Putnis 2009). Exsolution textures in the olivinites and clinopyroxenites include monticellite lamellae in forsterite (Fig. 2a), magnetite and magnesiohastingsite lamellae in diopside (Fig. 2b), and inclusions of spinel and ilmenite in Ti-rich magnetite (Fig. 2c, d).

Calcium is generally a minor constituent in forsterite, with concentrations lower than 1 wt% (Jurewicz and Watson 1988; Simkin and Smith 1970). The rare occurrence of Ca-rich exsolution phases, such as diopside and monticellite-kirschsteinite, have been reported as a product of postmagmatic transformation of olivine in terrestrial rocks (Gaeta 1996; Markl et al. 2001; Xiong et al. 2017; Yufeng et al. 2008) and meteorites (McKay et al. 1998; Mikouchi et al. 1995). We interpret the textures in the Afrikanda samples to have formed by exsolution of Fe-rich monticellite during postmagmatic equilibration of Ca-rich forsterite. Elongate lamellae of oxide phases in pyroxenes are observed in mafic igneous and metamorphic rocks (Fleet et al. 1980; Garrison and Taylor 1981). Based on petrographic evidence, we suggest that exsolution of Ti-rich magnetite and magnesiohastingsite from the diopside host at Afrikanda also occurred during subsolidus equilibration.

Magnetite is observed in both rock types, but the composition and homogeneity (i.e., the nature and relative abundance of exsolution lamellae) differs between the examined olivinite and clinopyroxenite samples. Exsolution textures in Ti-rich magnetite are common in mafic plutonic rocks and have been the subject of many researches (Haggerty 1991; Price 1980; Ramdohr 2013). Exsolution textures reflect the chemical composition and cooling history of the precursor magnetite (Buddington and Lindsley 1964; Howarth et al. 2013; Von Gruenewaldt et al. 1985). The magnetite in the olivinites has the highest concentrations of Ti, Mg and Al and does not exhibit any exsolution lamellae. Magnetite in the clinopyroxenite samples has much lower levels of these elements due to preferential partitioning of Ti and Mg into ilmenite, and Mg and Al into spinel inclusions (Fig. 2d). The variation in magnetite texture between the two rock types supports the suggestion that they underwent different degrees of subsolidus re-equilibration.

Perovskite textures in the silicocarbonatites

Chemical composition and zoning

Perovskite zoning in the silicocarbonatites is more complex than in the clinopyroxenites. The T2 perovskite has oscillatory zoning in the cores and irregular zoning at the rims (Fig. 5d) and in T3 massive perovskite has areas with oscillatory or irregular zoning, as well as homogeneous areas. The oscillatory zoning in T2 and T3 perovskite is a primary magmatic feature. The irregular complex zoning juxtaposed over primary growth patterns in these perovskite

varieties was caused by progressive infiltration of REE, Na and locally also Nb and Th into the structure during post-magmatic fluid-driven alteration (Chakhmouradian and Zaitsev 1999). This process culminated with the deposition of REE-perovskite and loparite-(Ce) locally along the margin of, and fractures within, perovskite crystals (Figs. 3d, 5c, d). Titanite crystallised after these minerals, indicating either an increase in silica activity, or a decrease in fluid temperature (Chakhmouradian 2004). The formation of symplectitic intergrowths of titanite with rutile and ilmenite (Fig. 2f) implies increasing fluid acidity or, more likely, a further decrease in temperature, which would expand the stability fields of both rutile and ilmenite at a given pH, $p(CO_2)$ and $a(Fe^{2+})$ (Chakhmouradian 2004; Chakhmouradian and Mitchell 2002).

Occasional grains of T2 perovskite rimmed by low-REE material are much less common and could be produced by the inverse process, i.e., extraction of REEs from perovskite by percolating fluids (Fig. 5c). The compositionally homogeneous sections in T3 perovskite probably re-equilibrated through solid-state diffusion, which erased such primary textural characteristics as growth zoning and multiphase inclusions.

Textural development

In the silicocarbonatites, we observe irregularly shaped crystals with continuous crystallographic orientation, similar to the clinopyroxenites; however, the small perovskite grains also have a single crystallographic orientation and are not a composite of subgrains (Fig. 4d_{iii}). The absence of EBSD evidence of subgrain coalescence and the preservation of oscillatory zoning in T2 and T3 perovskite suggests that the coarse-grained perovskite did not undergo the same coalescence and amalgamation processes as those observed in the ultramafic rocks. However, the similarities in chemical composition, zoning patterns and associated minerals [e.g., titanite, REE-perovskite and loparite-(Ce)] indicate that the perovskite from both the ultramafic rocks and silicocarbonatites experienced the same fluid-driven alteration. We propose that the silicocarbonatites did not undergo perovskite recrystallization due to the lower solidus temperature of the silicocarbonatites compared to the ultramafic rocks. Also, the perovskite was initially fine-grained in the olivinites and clinopyroxenites but coarse-grained in the silicocarbonatites, so the difference in initial grain size may have impeded perovskite re-crystallisation in the silicocarbonatites.

Textural similarities with other oxide deposits

Several textural features that support the process of perovskite amalgamation and re-equilibration in the Afrikanda complex are observed in other oxide-rich igneous systems, namely chromite and magnetite deposits (Charlier et al. 2006; Dill 2010; Mungall 2014), as well as mantle-derived lherzolites and dunites (Wandji et al. 2009), apatite in carbonatites (Chakhmouradian et al. 2017; Kamenetsky et al. 2015), recrystallized nepheline syenites (Chakrabarty et al. 2016; Ulbrich 1993) and magnesian-ilmenite xenolith/xenocrysts in kimberlites and basanites (Mitchell 1973; Leblanc et al. 1982). These features include granoblastic mosaics, massive textures, grain coarsening and the transition from inclusion-rich to inclusion-free grains (Christiansen 1985; Ghisler 1976; Yudovskaya and Kinnaird 2010). Understanding the mechanisms responsible for the development of these features in disseminated and massive ore bodies within chromitite and magnetitite layers remains ambiguous.

Granoblastic mosaics and massive textures

For comparison, we have chosen typical examples of ophiolite dunites, podiform chromitites and ultramafic xenoliths. Chains of connected euhedral chromite crystals observed in ultramafic xenoliths, igneous complexes like Bushveld (South Africa) and Fiskenaesset (Greenland) and the Oman ophiolite resemble networks of T1 perovskite (Fig. 10e). Granoblastic textures in peridotitic xenoliths from the subcontinental lithospheric mantle are highlighted by the equigranular, euhedral olivine with interspersed linear chromite chains (Fig. 10e, f). The latter are similar to the T1 perovskite chains at Afrikanda (Fig. 10b). The xenolith textures reflect metamorphic stresses that caused mineral grains to recrystallize into granoblastic mosaic textures with straight margins and 120° triple junctions (Pike and Schwarzman 1977). At Bushveld and Fisknaesset, small chromite grains are generally euhedral to subhedral and form elongate chains, also reminiscent of T1 perovskite (Ghisler 1970; Sampson 1932; Yudovskaya and Kinnaird 2010). Silicate mineral inclusions are common and mostly restricted to grain cores.

Chromitites in the Oman ophiolite belt demonstrate an increasing grain size with deformation (Christiansen 1986). Christiansen (1985) described three morphological types of chromite (A, B and C) that are comparable to the three textural types of perovskite (T1, T2 and T3), respectively, in the present study. Type A consists of closely packed subhedral to euhedral chromite grains that mostly range between 0.5 and 1 mm across and regularly host silicate inclusions. Type B is closely packed, subhedral to anhedral chromite grains between 0.1 mm and 4.5 mm in size with occasional silicate inclusions. Type C is composed of massive, closely packed and interlocking anhedral chromite grains with indiscernible boundaries and an estimated size larger than A- and B-type grains. Christiansen (1985, 1986) proposed that the coarsening of chromite occurred during recrystallization and

was driven by strain-induced grain boundary migration and/or grain growth driven by interfacial energy gradient. We suggest that a similar mechanism was responsible for the textural evolution of perovskite in the Afrikanda ultramafic rocks.

Chains of connected crystals with granoblastic-polygonal textures are also observed in disseminated magnetite ore from the Panzhihua layered mafic intrusion, China. In this intrusion, magnetite mostly forms net textures with densely packed clusters of polygonal grains with straight boundaries and 120° interfacial angles (Fig. 10c) that resemble the granoblastic texture of T1 perovskite (Figs. 1a, 3a, 10a; Pang et al. 2007; Zhou et al. 2005).

The presence of both inclusion-rich euhedral grains and inclusion-poor anhedral grains is also observed in chromitite layers from the Oman ophiolite belt and the Fiskenaesset and Bushveld complexes (Christiansen 1985; Ghisler 1976; Yudovskaya and Kinnaird 2010). The transition between these textures can be associated with late post-magmatic processes including re-equilibration, post-cumulus growth and contact metamorphism. The development of these inclusion-free grains and the associated massive textures at Afrikanda and other oxide deposits will be discussed in a subsequent publication.

No conclusive and/or unifying model has been proposed to explain the ore distributions and textural transformations observed in the aforementioned mineral deposits. Traditionally, the formation of oxide-rich seams, bands, stringers and layers has been linked to magmatic processes. Perovskite, chromite and magnetite deposits share textural features that could imply that their development involved similar mechanisms. As we suggest for perovskite in the Afrikanda alkaline–ultramafic complex, the initial crystallisation of oxide minerals (whether magmatic or not) is followed by their textural re-equilibration at subsolidus temperatures. This re-equilibration produces perceptible changes in the morphology, size, orientation and compositional homogeneity of oxide mineral grains. From an exploration standpoint, the most important outcome of these processes is the accumulation of early-formed crystals into high-density oxide-rich zones and their coarsening and "purification" to form high-grade mineralized zones.

Conclusions

The textural and chemical examination of perovskite from the olivinites, clinopyroxenites and silicocarbonatites in the Afrikanda alkaline–ultramafic complex revealed three types of perovskite (T1 to T3) and lead to the following conclusions:

1. Perovskite from olivinites, clinopyroxenite and silicocarbonatite yielded similar ages, with an average of 368.3 ± 1.2 Ma. The perovskite and titanite ages support the contemporaneous emplacement of these lithologies at Afrikanda. The ages are slightly younger than previously published ages and could be due to discrepancies associated with the technique or reflect the timing of recrystallization.
2. In ultramafic rocks (olivinites and clinopyroxenites), the progressive coarsening of perovskite from small, euhedral, disseminated grains into large anhedral and massive grains, and the various textures and zoning patterns is evidence of post-magmatic recrystallization and textural re-equilibration. We propose the post-magmatic development of perovskite involved three stages: (1) textural equilibration enabling the development of perovskite clusters and chains after initial perovskite crystallisation; (2) grain rotation and coalescence of the small equilibrated polygonal clusters to form larger anhedral polycrystalline mosaics; (3) in some areas the continued consolidation and coarsening transform the large polycrystalline perovskite into massive perovskite.
3. The textural similarities between perovskite from Afrikanda and chromite and magnetite layers in various igneous complexes suggest similar post-magmatic coarsening processes are also involved in the development of other oxide ore deposits with monomineralic layers.

Acknowledgements We thank the Geological Institute (the Kola Science Center of the Russian Academy of Sciences) in Apatity for donating Afrikanda samples for our study. We are grateful to Peter Downes and an anonymous reviewer, for their constructive comments and suggestions. Editorial handling by Ramya Murali is acknowledged. Financial support was provided by the Australian Research Council (Discovery Grant DP130100257, 2013–2015) and University of Tasmania (New Star Professorship, 2010–2014) to V. Kamenetsky.

References

Afanasyev BV (2011) Mineral resources of the alkaline–ultramafic massifs of the Kola Peninsula. Roza Vetrov, St. Petersburg, p 224 (in Russian)

Armbrustmacher TJ (1981) The Complex of Alkaline Rocks at Iron Hill, Powderhorn district, Gunnison County, Colorado. New Mexico Geological Society, New Mexico

Arzamastsev A, Wu F-Y (2014) U–Pb geochronology and Sr-Nd isotopic systematics of minerals from the ultrabasic-alkaline massifs of the Kola province. Petrology 22:462–479

Arzamastsev A, Glaznev V, Raevsky A, Arzamastseva L (2000) Morphology and internal structure of the Kola Alkaline intrusions, NE Fennoscandian shield: 3D density modelling and geological implications. J Asian Earth Sci 18:213–228

Barbosa ESR, Brod JA, Junqueira-Brod TC, Dantas EL, de Oliveira Cordeiro PF, Gomide CS (2012) Bebedourite from its type area

(Salitre I complex): a key petrogenetic series in the Late-Cretaceous Alto Paranaíba Kamafugite–Carbonatite–Phoscorite association. Cent Br Lithos 144:56–72
Borrok DM, Kelser SE, Boer RH, Essene EJ (1998) The Vergenoeg magnetite-fluorite deposit, South Africa; support for a hydrothermal model for massive iron oxide deposits. Econ Geol 93:564–586
Brod JA (1999) Petrology and geochemistry of the Tapira alkaline complex, Minas Gerais State, Brazil. Durham University, Durham
Buddington A, Lindsley D (1964) Iron-titanium oxide minerals and synthetic equivalents. J Petrol 5:310–357
Campbell LS, Henderson P, Wall F, Nielsen TF (1997) Rare earth chemistry of perovskite group minerals from the Gardiner complex. East Greenl Mineral Mag 61:197–212
Cawthorn R (2011) Geological interpretations from the PGE distribution in the Bushveld Merensky and UG2 chromitite reefs. J S Afr Inst Min Metall 111:67–79
Chakhmouradian AR (2004) Crystal chemistry and paragenesis of compositionally unique (Al-, Fe-, Nb-, and Zr-rich) titanite from Afrikanda, Russia. Am Mineral 89:1752–1762
Chakhmouradian AR, Mitchell RH (1997) Compositional variation of perovskite-group minerals from the carbonatite complexes of the Kola Alkaline Province, Russia. Can Mineral 35:1293–1310
Chakhmouradian AR, Mitchell RH (2000) Occurrence, alteration patterns and compositional variation of perovskite in kimberlites. Can Mineral 38:975–994
Chakhmouradian AR, Mitchell RH (2002) New data on pyrochlore-and perovskite-group minerals from the Lovozero alkaline complex, Russia. Eur J Mineral 14:821–836
Chakhmouradian A, Williams C (2004) Mineralogy of high-field-strength elements (Ti, Nb, Zr, Ta, Hf) in phoscoritic and carbonatitic rocks of the Kola Peninsula, Russia. Phoscorites Carbon Mantle Mine Key Example Kola Alkaline Province 10:293–340
Chakhmouradian AR, Zaitsev AN (1999) Calcite-amphibole-clinopyroxene rock from the Afrikanda complex, Kola Peninsula, Russia: mineralogy and a possible link to carbonatites. I Oxide minerals. Can Mineral 37:177–198
Chakhmouradian AR, Zaitsev AN (2002) Calcite–amphibole–clinopyroxene rock from the Afrikanda complex, Kola Peninsula, Russia: mineralogy and a possible link to carbonatites. III Silicate minerals. Can Mineral 40:1347–1374
Chakhmouradian AR, Zaitsev AN (2004) Afrikanda: an association of ultramafic, alkaline and alkali-silica-rich carbonatitic rocks from mantle-derived melts Phoscorites and carbonatites from mantle to mine: the key example of the Kola Alkaline Province. Mineral Soc UK Ser 10:247–291
Chakhmouradian A, Mitchell R, Pankov A, Chukanov N (1999) Loparite and 'metaloparite' from the Burpala alkaline complex, Baikal Alkaline Province (Russia). Mineral Mag 63:519–519
Chakhmouradian AR, Cooper MA, Medici L, Hawthorne FC, Adar F (2008) Fluorine-rich hibschite from silicocarbonatite, Afrikanda complex, Russia: crystal chemistry and conditions of crystallization. Can Mineral 46:1033–1042
Chakhmouradian AR, Reguir EP, Kamenetsky VS, Sharygin VV, Golovin AV (2013) Trace-element partitioning in perovskite: implications for the geochemistry of kimberlites and other mantle-derived undersaturated. Rocks Chem Geol 353:112–131
Chakhmouradian AR et al (2017) Apatite in carbonatitic rocks: compositional variation, zoning, element partitioning and petrogenetic significance. Lithos 274:188–213
Chakrabarty A, Mitchell R, Ren M, Saha P, Pal S, Pruseth K, Sen A (2016) Magmatic, hydrothermal and subsolidus evolution of the agpaitic nepheline syenites of the Sushina Hill Complex, India: implications for the metamorphism of peralkaline syenites. Mineral Mag 80:1161–1193
Charlier B, Duchesne J-C, Vander Auwera J (2006) Magma chamber processes in the Tellnes ilmenite deposit (Rogaland Anorthosite Province, SW Norway) and the formation of Fe–Ti ores in massif-type anorthosites. Chem Geol 234:264–290
Christiansen F (1985) Deformation fabric and microstructures in ophiolitic chromitites and host ultramafics, Sultanate of Oman. Geologische Rundschau 74:61–76
Christiansen FG (1986) Deformation of chromite: SEM investigations. Tectonophysics 121:175–196
Clark BR, Price FR, Kelly WC (1977) Effects of annealing on deformation textures in galena. Contrib Miner Petrol 64:149–165
Dawson J, Hawthorn J (1973) Magmatic sedimentation and carbonatitic differentiation in kimberlite sills at Benfontein, South Africa. J Geol Soc 129:61–85
Dill HG (2010) The "chessboard" classification scheme of mineral deposits: Mineralogy and geology from aluminum to zirconium. Earth Sci Rev 100:1–420
Doherty R et al (1997) Current issues in recrystallization: a review. Mater Sci Eng A 238:219–274
Dowty E (1976a) Crystal structure and crystal growth: I. The influence of internal structure on morphology. Am Miner 61:448–459
Dowty E (1976b) Crystal structure and crystal growth: II. Sect Zon Miner Am Mineral 61:460–469
Eales H, Costin G (2012) Crustally contaminated komatiite: primary source of the chromitites and Marginal, Lower, and Critical Zone magmas in a staging chamber beneath the Bushveld. Complex Econ Geol 107:645–665
Eales H, De Klerk W, Teigler B (1990) Evidence for magma mixing processes within the Critical and Lower Zones of the northwestern Bushveld Complex. S Afr Chem Geol 88:261–278
Fleet M, Bilcox GA, Barnett RL (1980) Oriented magnetite inclusions in pyroxenes from the Grenville Province. Can Mineral 18:89–99
Force ER (1991) Geology of titanium-mineral deposits, vol 259. Geological Society of America, New York
Gaeta M (1996) Ca–Fe-rich exsolution lamellae from olivine in a wehrlitic xenolith, Monti Vulsini Volcanic District, Central Italy. Mineral Petrol Acta 39:159–167
Garrison JR, Taylor LA (1981) Petrogenesis of pyroxene-oxide intergrowths from kimberlite and cumulate rocks; co-precipitation or exsolution? Am Miner 66:723–740
Ghisler M (1970) Pre-metamorphic folded chromite deposits of stratiform type in the early Precambrian of West, Greenland. Mineral Depos 5:223–236
Ghisler M (1976) The geology, mineralogy and geochemistry of the-Pre-Orogenic Archaean stratiform chromite deposits at-Fiskenaesset, West Greenland
Haggerty SE (1991) Oxide textures; a mini-atlas. Rev Mineral Geochem 25:129–219
Harlov DE, Meighan CJ, Kerr ID, Samson IM (2016) Mineralogy, chemistry, and fluid-aided evolution of the Pea Ridge Fe oxide-(Y + REE) deposit, southeast Missouri, USA. Econ Geol 111:1963–1984
Herz N (1976) Titanium deposits in alkalic igneous rocks. US Department of the Interior, Geological Survey, New York
Higgins MD (2011) Textural coarsening in igneous rocks. Int Geol Rev 53:354–376
Higgins MD (2015) Quantitative textural analysis of rocks in layered mafic intrusions. In: Layered Intrusions. Springer, pp 153–181
Higgins MD (2017) Quantitative investigation of felsic rock textures using cathodoluminescence images and other techniques. Lithos 277:259–268
Holm E, Farjami S, Manohar P, Rohrer G, Rollett A, Srolovitz D, Weiland H (2016) Proceedings of the 6th International Conference on Recrystallization and Grain Growth (ReX&GG 2016). Springer

Holness MB, Cheadle MJ, McKenzie D (2005) On the use of changes in dihedral angle to decode late-stage textural evolution in cumulates. J Petrol 46:1565–1583

Holness MB, Nielsen TF, Tegner C (2006) Textural maturity of cumulates: a record of chamber filling, liquidus assemblage, cooling rate and large-scale convection in mafic layered intrusions. J Petrol 48:141–157

Horstwood MS et al (2016) Community-derived standards for LA-ICP-MS U-(Th-) Pb geochronology–uncertainty propagation, age interpretation and data reporting. Geostand Geoanal Res 40:311–332

Hou B, Keeling J, Van Gosen BS (2017) Geological and exploration models of beach placer deposits, integrated from case-studies of Southern Australia. Ore Geol Rev 80:437–459

Howarth GH, Prevec SA, Zhou M-F (2013) Timing of Ti-magnetite crystallisation and silicate disequilibrium in the Panzhihua mafic layered intrusion: Implications for ore-forming processes. Lithos 170:73–89

Humphreys F (2001) Review grain and subgrain characterisation by electron backscatter diffraction. J Mater Sci 36:3833–3854

Humphreys FJ, Hatherly M (2004) Recrystallization and related annealing phenomena. Elsevier, Amsterdam

Hunter RH (1987) Textural equilibrium in layered igneous rocks. In: Origins of igneous layering. Springer, pp 473–503

Irvine T (1977) Origin of chromitite layers in the Muskox intrusion and other stratiform intrusions: a new interpretation. Geology 5:273–277

Jones A, Ralph B, Hansen N (1979) Subgrain coalescence and the nucleation of recrystallization at grain boundaries in aluminium. Proc R Soc Lond 368:345–357

Jurewicz AJ, Watson EB (1988) Cations in olivine, Part 1: Calcium partitioning and calcium-magnesium distribution between olivines and coexisting melts, with petrologic applications. Contrib Mineral Petrol 99:176–185

Kamenetsky VS, Mitchell RH, Maas R, Giuliani A, Gaboury D, Zhitova L (2015) Chlorine in mantle-derived carbonatite melts revealed by halite in the St.-Honoré intrusion (Québec, Canada). Geology 43:687–690

Kinnaird J, Kruger F, Nex P, Cawthorn R (2002) Chromitite formation—a key to understanding processes of platinum enrichment. Appl Earth Sci 111:23–35

Knipping JL et al (2015) Trace elements in magnetite from massive iron oxide-apatite deposits indicate a combined formation by igneous and magmatic-hydrothermal processes. Geochim Cosmochim Acta 171:15–38

Kolker A (1982) Mineralogy and geochemistry of Fe–Ti oxide and apatite (nelsonite) deposits and evaluation of the liquid immiscibility hypothesis. Econ Geol 77:1146–1158

Kramm U, Kogarko L, Kononova V, Vartiainen H (1993) The Kola Alkaline province of the CIS and Finland: Precise Rb-Sr ages define 380–360 Ma age range for all magmatism. Lithos 30:33–44

Kreitcberg A, Brailovski V, Turenne S (2017) Effect of heat treatment and hot isostatic pressing on the microstructure and mechanical properties of Inconel 625 alloy processed by laser powder bed fusion. Mater Sci Eng A 689:1–10

Kretz R (1966) Interpretation of the shape of mineral grains in metamorphic rocks. J Petrol 7:68–94

Kukharenko AA et al (1965) The Caledonian complex of ultrabasic and alkaline rocks and carbonatites of the Kola Peninsula and Northern Karelia. Nedra, Leningrad

Latypov R, O'Driscoll B, Lavrenchuk A (2013) Towards a model for the in situ origin of PGE reefs in layered intrusions: insights from chromitite seams of the Rum Eastern Layered Intrusion, Scotland. Contrib Mineral Petrol 166:309–327

Latypov R, Chistyakova S, Mukherjee R (2017) A novel hypothesis for origin of massive Chromitites in the bushveld igneous complex. J Petrol 1:41

Leblanc M, Dautria J-M, Girod M (1982) Magnesian ilmenitite xenoliths in a basanite from Tahalra, Ahaggar (Southern Algeria). Contrib Miner Petrol 79:347–354

Li JC (1962) Possibility of subgrain rotation during recrystallization. J Appl Phys 33:2958–2965

Lister GF (1966) The composition and origin of selected iron-titanium deposits. Econ Geol 61:275–310

Markl G, Marks M, Wirth R (2001) The influence of T, $aSiO_2$, and fO_2 on exsolution textures in Fe–Mg olivine: an example from augite syenites of the Ilimaussaq Intrusion, South Greenland. Am Mineral 86:36–46

McCloy J, Korenstein R, Zelinski B (2009) Effects of temperature, pressure, and metal promoter on the recrystallized structure and optical transmission of chemical vapor deposited zinc sulfide. J Am Ceram Soc 92:1725–1731

McDonald JA (1965) Liquid immiscibility as one factor in chromitite seam formation in the Bushveld Igneous complex. Econ Geol 60:1674–1685

McKay G, Miyamoto M, Mikouchi T, Ogawa T (1998) The cooling history of the Lewis Cliff 86010 angrite as inferred from kirschsteinite lamellae in olivine. Meteorit Planet Sci 33:977–983

Mikouchi T, Takeda H, Miyamoto M, Ohsumi K, McKay GA (1995) Exsolution lamellae of kirschsteinite in magnesium-iron olivine from an angrite meteorite. Am Mineral 80:585–592

Mitchell RH (1973) Magnesian ilmenite and its role in kimberlite petrogenesis. J Geol 81:301–311

Mitchell RH, Welch MD, Chakhmouradian AR (2017) Nomenclature of the perovskite supergroup: a hierarchical system of classification based on crystal structure and composition. Mineral Mag 81:411–462

Mondal SK, Mathez EA (2006) Origin of the UG2 chromitite layer Bushveld Complex. J Petrol 48:495–510

Mungall J (2014) Geochemistry of magmatic ore deposits. In: Treatise on geohemistry, vol 13. 2 edn, pp 195–218

Nielsen T (1980) The petrology of a melilitolite, melteigite, carbonatite and syenite ring dike system, in the Gardiner complex, East Greenland Lithos 13:181–197

Nielsen TFD, Solovova IP, Veksler IV (1997) Parental melts of melilitolite and origin of alkaline carbonatite: evidence from crystallised melt inclusions Gardiner complex. Contrib Mineral Petrol 126:331–344

Pang K-N, Zhou M-F, Lindsley D, Zhao D, Malpas J (2007) Origin of Fe–Ti oxide ores in mafic intrusions: evidence from the Panzhihua intrusion SW China. J Petrol 49:295–313

Pekov I, Petersen OV, Voloshin A (1997) Calcio-ancylite-(Ce) from Ilímaussaq and Narssârssuk, Greenland, Kola Peninsula and Polar Urals, Russia, ancylite-(Ce)-calcio-ancylite-(Ce) an isomorphous series. Neues Jahrbuch für Minerologie, Abhandlungen 171(3):309–322

Pike JN, Schwarzman E (1977) Classification of textures in ultramafic xenoliths. J Geol 85:49–61

Price G (1980) Exsolution microstructures in titanomagnetites and their magnetic significance. Phys Earth Planet Int 23:2–12

Pushkarev E, Kamenetsky V, Morozova A, Khiller V, Glavatskykh S, Rodemann T (2015) Ontogeny of ore Cr-spinel and composition of inclusions as indicators of the pneumatolytic–hydrothermal origin of PGM-bearing chromitites from Kondyor massif, the Aldan Shield. Geol Ore Deposit 57:352–380

Putnis A (2009) Mineral replacement reactions. Rev Mineral Geochem 70:87–124

Ramdohr P (2013) The ore minerals and their intergrowths. Elsevier, Amsterdam

Reguir EP, Camacho A, Yang P, Chakhmouradian AR, Kamenetsky VS, Halden NM (2010) Trace-element study and uranium-lead dating of perovskite from the Afrikanda plutonic complex, Kola Peninsula (Russia) using LA-ICP-MS. Miner Petrol 100:95–103

Rios PR, Siciliano F Jr, Sandim HRZ, Plaut RL, Padilha AF (2005) Nucleation and growth during recrystallization. Mater Res 8:225–238

Salnikova E, Stifeeva M, Chakhmouradian A, Glebovitsky V, Reguir E (2018) The U–Pb system in schorlomite from calcite–amphobole–pyroxene Pegmatite of the Afrikanda Complex (Kola Peninsula). Dokl Earth Sci 478:148–151

Sampson E (1932) Magmatic chromite deposits in southern Africa. Econ Geol 27:113–144

Sandström R, Lehtinen B, Hedman E, Groza I, Karlsson S (1978) Subgrain growth in Al and Al-1% Mn during annealing. J Mater Sci 13:1229–1242

Simkin T, Smith J (1970) Minor-element distribution in olivine. J Geol 78:304–325

Stacey JS, Kramers JD (1975) Approximation of terrestrial lead isotope evolution by a two-stage model. Earth Planet Sci Lett 26:207–221

Syrenko A, Klinishev G (1973) Recrystallization of copper under hydrostatic pressure up to 15 kbar. J Mater Sci 8:765–769

Ulbrich MN (1993) Mineralogy of nepheline syenites from the Poços de Caldas alkaline massif SE Brazil: chemistry, X-ray data and microtextures of feldspars. Revista Brasileira de Geociências 23:388–399

Varma S, Willits BL (1984) Subgrain growth in aluminum during static annealing. Metal Trans A 15:1502–1503

Vernon R (1970) Comparative grain-boundary studies of some basic and ultrabasic granulites, nodules and cumulates Scottish. J Geol 6:337–351

Vidyashankar H, Govindaiah S (2009) Ore petrology of the V-Ti magnetite (lodestone) layers of the Kurihundi area of Sargur schist belt, Dharwar craton. J Geol Soc India 74:58–68

Von Gruenewaldt G, Klemm D, Henckel J, Dehm R (1985) Exsolution features in titanomagnetites from massive magnetite layers and their host rocks of the Upper Zone, Eastern Bushveld Complex. Econ Geol 80:1049–1061

Vukmanovic Z, Barnes SJ, Reddy SM, Godel B, Fiorentini ML (2013) Morphology and microstructure of chromite crystals in chromitites from the Merensky Reef (Bushveld Complex, South Africa). Contrib Miner Petrol 165:1031–1050

Walter J, Koch E (1963) Substructures and recrystallization of deformed (100)[001]-oriented crystals of high-purity silicon-iron. Acta Metall 11:923–938

Wandji P, Tsafack J, Bardintzeff J, Nkouathio D, Dongmo AK, Bellon H, Guillou H (2009) Xenoliths of dunites, wehrlites and clinopyroxenites in the basanites from Batoke volcanic cone (Mount Cameroon, Central Africa): petrogenetic implications. Miner Petrol 96:81–98

Wu F-Y, Yang Y-H, Mitchell RH, Bellatreccia F, Li Q-L, Zhao Z-F (2010) In situ U–Pb and Nd–Hf–(Sr) isotopic investigations of zirconolite and calzirtite. Chem Geol 277:178–195

Wu F-Y, Arzamastsev AA, Mitchell RH, Li Q-L, Sun J, Yang Y-H, Wang R-C (2013) Emplacement age and Sr–Nd isotopic compositions of the Afrikanda alkaline ultramafic complex, Kola Peninsula, Russia. Chem Geol 353:210–229

Xiong F, Yang J, Dilek Y, Wang C (2017) Nanoscale diopside and spinel exsolution in olivine from dunite of the tethyan ophiolites, Southwestern Turkey: implications for the multi-stage process. J Nanosci Nanotechnol 17:6587–6596

Yudin B, Zak S (1971) Titanium deposits of northwestern USSR (eastern part of Baltic Shield). Int Geol Rev 13:864–872

Yudovskaya MA, Kinnaird JA (2010) Chromite in the Platreef (Bushveld Complex, South Africa): occurrence and evolution of its chemical composition. Miner Depos 45:369–391

Yufeng R, Fangyuan C, Jingsui Y, Yuanhong G (2008) Exsolutions of diopside and magnetite in olivine from mantle dunite, Luobusa ophiolite, Tibet, China. Acta Geol Sin English Ed 82:377–384

Zaitsev AN, Chakhmouradian AR (2002) Calcite–amphibole–clinopyroxene rock from the Afrikanda complex, Kola Peninsula, Russia: mineralogy and a possible link to carbonatites. II Oxysalt minerals. Can Mineral 40:103–120

Zhou M-F, Robinson PT, Lesher CM, Keays RR, Zhang C-J, Malpas J (2005) Geochemistry, petrogenesis and metallogenesis of the Panzhihua gabbroic layered intrusion and associated Fe–Ti–V oxide deposits, Sichuan Province, SW China. J Petrol 46:2253–2280